

Tracing Earth's Volatile Delivery With Tin

E. Kubik, J. Siebert, B. Mahan, J. Creech, I. Blanchard, A. Agranier, S. Shcheka, F. Moynier

▶ **To cite this version:**

E. Kubik, J. Siebert, B. Mahan, J. Creech, I. Blanchard, et al.. Tracing Earth's Volatile Delivery With Tin. Journal of Geophysical Research : Solid Earth, 2021, 126, 12 pp. 10.1029/2021JB022026 . insu-03589890

HAL Id: insu-03589890

https://insu.hal.science/insu-03589890

Submitted on 3 Mar 2022

HAL is a multi-disciplinary open access archive for the deposit and dissemination of scientific research documents, whether they are published or not. The documents may come from teaching and research institutions in France or abroad, or from public or private research centers.

L'archive ouverte pluridisciplinaire **HAL**, est destinée au dépôt et à la diffusion de documents scientifiques de niveau recherche, publiés ou non, émanant des établissements d'enseignement et de recherche français ou étrangers, des laboratoires publics ou privés.

Copyright

Check for updates

JGR Solid Earth

RESEARCH ARTICLE
10.1029/2021JB022026

Tracing Earth's Volatile Delivery With Tin

E. Kubik[1], J. Siebert[1,2], B. Mahan[1], J. Creech[1], I. Blanchard[3], A. Agranier[4], S. Shcheka[3], and F. Moynier[1,2]

[1]Université de Paris, Institut de Physique du Globe de Paris, CNRS, Paris, France, [2]Institut Universitaire de France, Paris, France, [3]Bayerisches Geoinstitut, University of Bayreuth, Bayreuth, Germany, [4]Institut Universitaire Européen de la Mer, University of Brest, Plouzané, France

Key Points:

- Sn is very siderophile at high pressure, requiring a volatile delivery in the last 10% of accretion for its mantle signature to be explained
- Sn isotope fractionation results indicate that core formation may generate a mantle significantly lighter than the core and building blocks
- The most likely source of volatile elements is carbonaceous chondrite-like material

Supporting Information:

Supporting Information may be found in the online version of this article.

Correspondence to:

E. Kubik,
kubik@ipgp.fr

Citation:

Kubik, E., Siebert, J., Mahan, B., Creech, J., Blanchard, I., Agranier, A., et al. (2021). Tracing Earth's volatile delivery with tin. *Journal of Geophysical Research: Solid Earth*, *126*, e2021JB022026. https://doi.org/10.1029/2021JB022026

Received 11 MAR 2021
Accepted 18 AUG 2021

Abstract Earth's accretion history for volatile elements, and the origin of their depletions with respect to the Sun and primitive meteorites, continue to be debated. Two end-member scenarios propose either that volatile elements were delivered during the main phases of accretion and differentiation, or that the Earth accreted from materials largely devoid of volatiles with late addition of volatile-rich materials. Experiments evaluating the effect of metal–silicate equilibrium on elemental and isotopic distribution of volatile and siderophile elements such as Sn can help to distinguish between these scenarios. In this study, we have systematically investigated the relative influence of temperature, pressure, oxygen fugacity, and metal and silicate composition on the metal–silicate partioning behavior of Sn, from 2 to 20 GPa and 1,700 to 2,573 K, indicating that Sn siderophility noticeably decreases with temperature and S content of the metal but increases dramatically with pressure. A resolvable isotopic fractionation factor between metal and silicate suggests that core–mantle equilibrium temperatures (~3,000 K) could potentially generate a Sn isotopic composition of the mantle lighter than the core by 150–200 ppm/amu. Core formation modeling shows that the volatiles were added during the last 10% of the accretion history. A final core containing 2.5 to 3.5 wt.% S is required. Furthermore, modeling of the BSE isotopic composition argues for a late Sn delivery on Earth with carbonaceous chondrite-like material as the most likely source of volatiles. Therefore, both elemental and isotopic approaches converge toward an identical volatile accretion scenario, involving a late volatile delivery.

Plain Language Summary The timing of delivery of volatile elements—elements requiring low temperatures to be present at condensed states—has extensive implications regarding fundamental questions in Earth and life sciences, such as when a planet becomes habitable. Volatile elements can be siderophile (iron-loving), meaning that they have an affinity for the core. The differentiation of the Earth into a core and a mantle redistributed these elements between both reservoirs. We quantified the affinity of Sn for the core relative to the mantle by equilibrating a silicate with a metal, behaving as anologues of the mantle and core respectively. Expected mantle abundances were computed for different accretion scenarios, including a volatile delivery (a) during the entirety of Earth's accretion, (b) during the last steps of the accretion, and (c) after core formation ceased. Our experiments suggest that core formation may induce preferential segregation of lighter Sn isotopes in the mantle with respect to the core. Results for Sn elemental and isotopic behavior during differentiation both converge to a volatile delivery during the last 10% of accretion. Tin isotopes can be used to discriminate between several precursors and we find that carbonaceous chondrites—a type of primitive meteorites—are the most likely source of Earth's volatile elements.

1. Introduction

The habitability of Earth depends intrinsically on the presence of volatile elements, and therefore the timing and origin of volatile elements delivery to Earth is a key question, yet to be answered. Volatile elements are depleted in terrestrial planets compared to the Sun's photosphere with degree of depletion generally increasing with decreasing condensation temperature (Palme & O'Neill, 2013). The two most extreme mechanisms that could explain this depletion are (a) a loss of volatile elements by syn- and post-accretion volatilization processes, or (b) a depletion of volatile elements within the accreted material that formed the terrestrial planets due to incomplete condensation in the solar nebula (Albarède, 2009).

© 2021. American Geophysical Union. All Rights Reserved.

A lack of K (Bloom et al., 2020; Humayun & Clayton, 1995; Tuller-Ross et al., 2019; Wang & Jacobsen, 2016), Rb (Nebel et al., 2011; Pringle & Moynier, 2017) and Zn (Luck et al., 2005; Pringle et al., 2017; Sossi et al., 2017) heavy isotope enrichment in the Earth's mantle compared to primitive meteorites has been used as evidence for the absence of volatile loss by evaporation during Earth's formation. Furthermore, the Mn/Na ratio, which is a tracer of post-nebular volatilization, is roughly chondritic in the Earth, suggesting limited volatile loss during or after Earth's accretion (O'Neill & Palme, 2008; Siebert et al., 2018). However, it should be noted that small isotopic fractionations observed for Mg (Hin et al., 2017) and Si (e.g., Pringle et al., 2014; Young et al., 2019) have been used as argument that volatilization may play a role in establishing the composition of the Earth. The same is not true for the Moon and some other differentiated terrestrial bodies, which are markedly enriched in the heavy isotopes of numerous elements (Boyce et al., 2015; Kato et al., 2015; Nie & Dauphas, 2019; Pringle et al., 2014; Pringle & Moynier, 2017; Sharp et al., 2010; Wang et al., 2019; Wang & Jacobsen, 2016), or light isotopes for certain elements (e.g., Cr, Sn; Sossi et al., 2018; Wang et al., 2019), lending creedence to the widely held view that volatilization during Moon formation and evolution resulted in isotopic fractionation. This study focuses on the accretion of volatile elements during Earth's formation, the nature of its building blocks, and subsequent core–mantle differentiation. Several accretion scenarios could produce the observed volatile elements pattern of the Earth:

1. The Earth formed from material largely devoid of volatile elements, a.k.a. “dry accretion.” This scenario is supported by the fact that the solar system temperature during the main phases of Earth's accretion may be too high to allow the condensation of those elements (Albarède, 2009). In this case, the volatiles are brought after the planet's differentiation ceased around 100 million years after the solar system formation, as the so-called late veneer (Albarède et al., 2013; O'Neill, 1991; Wang & Becker, 2013).
2. In a second possible scenario, the Earth is accreted from material partially depleted in volatile elements, such as chondrites or their components (e.g., chondrules). The subsequent differentiation redistributes the elements according to their siderophile behavior between core and mantle (Righter et al., 2017; Wood & Halliday, 2010) or are lost by evaporation (Hin et al., 2017; Norris & Wood, 2017; Pringle et al., 2014). In this case, volatiles are mostly brought during the main phases of the planet's accretion.
3. A third and intermediate scenario consists of the heterogeneous accretion of the planet, where the volatile elements are mainly brought during the last phases of accretion and differentiation. It has been recently proposed that volatile elements on Earth come from 10 to 15 wt.% of CI-like material brought in the later part of the main phases of Earth's accretion (Braukmüller et al., 2019; Budde et al., 2019; Hopp et al., 2020; Kubik et al., 2021; Mahan, Siebert, Blanchard, Badro, et al., 2018, Mahan, Siebert, Blanchard, Borensztajn, et al., 2018). Volatiles are accreted rapidly and late, possibly associated with the formation of the so-called Hadean matte (O'Neill, 1991; Savage et al., 2015; Schonbachler et al., 2010), a sulfur- and volatile-rich liquid that settles at the core–mantle boundary and subsequently mixes into the core.

The study of the partitioning and isotopic behavior of elements that are both volatile and siderophile can help discriminate between these three scenarios by isolating the effect of siderophile processes, such as the Earth's differentiation, from the effect of volatile processes.

Moderately siderophile and volatile elements (MSVEs) are depleted in the Earth's mantle compared to lithophile volatile elements, presumably due to their segregation into the core, and as a consequence they do not follow the canonical volatility trend pattern (Lodders, 2003; Wasson et al., 1988; Wood et al., 2019). A way to infer the effect of differentiation on the observed volatile depletion is to experimentally study the behavior of MSVEs during such processes (e.g., Ballhaus et al., 2017; Blanchard et al., 2015; Corgne et al., 2008; Kubik et al., 2021; Mahan et al., 2017; Mahan, Siebert, Blanchard, Badro, et al., 2018; Mahan, Siebert, Blanchard, Borensztajn, et al., 2018; Righter et al., 2017; Siebert et al., 2011; Steenstra et al., 2016; 2017; 2019; Suer et al., 2017). The behavior of MSVEs at core formation conditions in controlled experiments, and their comparison to geochemical observables, helps to deconvolve the effects of differentiation and volatile-related processes from one another. Two different approaches—elemental, and isotopic—can be used to investigate such behavior.

The elemental behavior of the MSVEs can be experimentally characterized at metal–silicate equilibrium, wherein metal–silicate partition coefficients are measured to express the MSVE fractionation between the metal and silicate phases. Comprehensive parameterization of metal–silicate partitioning constrains the effect of temperature, pressure, fO_2, metal and silicate composition (including the influence of capsule material) (Siebert et al., 2011).

Numerous recent studies investigated the metal–silicate isotopic fractionation of elements (e.g., Bourdon et al., 2018; Burkhardt et al., 2014; Creech, Baker, et al., 2017; Hin et al., 2014; Mahan et al., 2017; Savage et al., 2015; Shahar et al., 2015). In such studies, experimental metal–silicate fractionations of a given element are often compared to the isotopic composition of the bulk silicate Earth (BSE) and primitive meteorites to assess whether the siderophile element signature in the Earth's mantle can be explained by the accretion and differentiation of primitive material from the solar system. Measurements of isotopic fractionation provide a second and independent constraint on the timing and origin of the volatile accretion relative to the Earth's differentiation, and likewise comparison to the BSE and primitive meteorites provides insights into dominant redistribution processes and source materials.

Combining elemental and isotopic observations from experiments is thus a particularly robust approach, where parameterisations of elemental and isotopic fractionations between metal and silicate can be used as input in core formation models. In such models, the partitioning and isotopic fractionation can be reconstructed at each step of the Earth's accretion, taking into account the evolving pressure and temperature conditions, allowing to test different accretion scenarios and address questions regarding the formation and differentiation of terrestrial planets (e.g., Blanchard et al., 2015; Bourdon et al., 2018; Kubik et al., 2021; Rubie et al., 2011; Rudge et al., 2010; Wade & Wood, 2005). In particular, this approach has allowed to determine the pressure, temperature and oxygen fugacity conditions of core formation (e.g., Wade & Wood, 2005). The results of those models can then be compared to natural observations and used to discriminate between accretion scenarios.

In this study we have comprehensively characterized Sn partitioning and isotopic fractionation at metal–silicate equilibrium. Tin is a moderately siderophile and moderately volatile element with a condensation temperature of 704 K (Lodders, 2003) recently reappraised to 604 K according to Wood et al. (2019). As such, Sn abundance in the Earth's mantle is affected by both core–mantle differentiation and by volatile processes, which makes it a good tracer of volatile accretion. Tin's depletion in Earth's primitive mantle by a factor of five (relative to the canonical volatility trend) is very small compared to the depletion expected from its siderophile behavior at low pressure and low temperature. For example, Sn's metal–silicate partitioning at low P, T conditions is very close to that of S, however Sn is less depleted in the Earth's mantle than S by a factor of 20 (Palme & O'Neill, 2013; Wood et al., 2006). By characterizing Sn partitioning at the conditions of Earth's accretion, it is possible to constrain possible accretion pathways that can lead to this perceived overabundance. This study is focused on Sn and expands the conditions of investigation of Sn metal–silicate partitioning behavior, in particular by applying higher pressures than most previous studies (Ballhaus et al., 2013, 2017; Capobianco et al., 1999; Righter et al., 2010, 2017, 2019; Righter & Drake, 2000; Vogel et al., 2018). By focusing explicitly on Sn and its partitioning at higher P, T conditions than previously explored, we provide comprehensive constraints on its partitioning as a function of thermodynamic variables. Novel partitioning results from 30 metal–silicate experiments have been combined with literature data for parameterization of Sn partitioning at P, T conditions that encompass those during Earth's core–mantle differentiation, and this has been input into models of Sn partitioning at plausible core formation conditions.

Tin has 10 stable isotopes with masses ranging from 112 to 124. The most abundant are ^{120}Sn (32.6%), ^{118}Sn (24.2%) and ^{116}Sn (14.5%). The observation of Sn isotopic fractionation during igneous processes (Badullovich et al., 2017; Wang et al., 2018) is a good indicator that it might also fractionate between molten metal and silicate. For now, no data exist on Sn isotopic fractionation in this context. Recent study by Creech and Moynier (2019) report Sn isotopic compositions for a selection of ordinary, enstatite and carbonaceous chondrites. These three chondrite types show distinct Sn isotopic compositions, with average $\delta^{122/118}$Sn (permil variation of the ^{122}Sn/^{118}Sn ratio relative to the IPGP_Sn standard) of -0.29 ± 0.44‰, 0.12 ± 0.28‰, and 0.47 ± 0.12‰, respectively. Furthermore, an overlap between the carbonaceous chondrites measurements and the BSE, which has a $\delta^{122/118}$Sn equal to 0.49 ± 0.11‰ (Badullovich et al., 2017), is observed. Therefore, comparing the isotopic fractionation of Sn as a consequence of metal–silicate differentiation to the Sn isotopic composition of chondrites may help discriminate between possible source materials for Earth's volatiles. Moreover, it has recently been shown that the silicate Moon is enriched in the lighter isotopes of Sn compared to the silicate Earth as a result of volatility processes (Wang et al., 2019). As it has been suggested that most of the missing lunar Sn may alternatively be stored in its core (Steenstra et al., 2016), it is important to test whether part of the light isotope enrichment of the lunar mantle may

Table 1
Starting Materials Compositions (wt.%)

	Silicate phase		Metallic phase				
Starting material	MORB	KLB1	Sn	Fe	FeS	Cu	Tl, In, Cd, Bi, Sb
A	70%		8%	22%			
B	70%		4%	26%			
C	70%		4%	13%	13%		
D	70%		4%	25%		1%	
E		70%	4%	25%		1%	
F	70%		2%	30%		1%	1% of each
G	70%		2%	13.5%	16.5%	1%	1% of each

reflect metal–silicate fractionation. It should be noted that Sn fractionation during volatilization processes has been evidenced both from low temperature experimental study (She et al., 2019) and natural sample measurements (Creech et al., 2019).

2. Experimental and Analytical Methods

2.1. Starting Materials

Seven mixtures composed of homogenised metallic and silicate powders were used to conduct the 30 high-pressure and high-temperature experiments of this study (Table 1). The different compositions of the metallic and silicate phases were used to experimentally assess their effect on partitioning and isotopic fractionation. The material was Sn doped from 2 to 8 wt.% using Putratronic pure 99.8% powder to ensure sufficient Sn concentration in the silicate for electron microprobe measurement. Three additional experiments were doped with 2, 5, and 10 wt.% of Si in order to investigate the effect of Si on Sn partitioning and widen the range of fO_2 of this study.

2.2. Piston Cylinder Experiments

Eighteen experiments were performed using a 150 ton end-loaded piston cylinder apparatus at the Institut de Physique du Globe de Paris (IPGP). All piston cylinder experiments conducted in this study were performed at 2 GPa and from 1696 to 2296 K. Those conditions allowed the fusion of the material and the equilibrium between metal and silicate. Two capsule materials were tested, boron nitride and magnesium oxide, in order to study the interaction processes that could occur during the experiment. The metal and silicate were separated and sufficient material from each phase was prepared for both elemental and isotopic analysis. Clean pieces were carefully selected mechanically under magnifying glass.

2.3. Multianvil Experiments

Twelve experiments were performed at Bayerisches Geoinstitut using a 5,000 ton Zwick and a 1,000 ton Hymag multianvil apparatus from 7 to 20 GPa. The starting material was contained in a single-crystal MgO capsule and lid. During the experiment, the sample temperature was monitored using a $W_{97}Re_3/W_{75}Re_{25}$ type D thermocouple. All experimental parameters are summarized in Table 2. More details about the experimental protocol, parameters that were used and the calibration of the instruments can be found in the Supporting Information S1.

2.4. Electron Microprobe Analysis

Pieces of metal and silicate from each experiment were selected, mounted in a resin and polished. Those pieces were then carbon coated and analyzed with the CAMPARIS laboratory CAMECA SX Five electron microprobe (Université Pierre et Marie Curie) in order to resolve a selection of major and trace elements in both metal and silicate phases (Table 2). To avoid any effect of the quenched textures obtained in the experiments on the microprobe analysis, especially in the metal parts, rasters of 30 μm were used instead of points. No zonations were found across the sample in each experiment, which proves that elemental equilibrium was achieved. Analysis parameters as well as the nature of the standards are described in the Supporting Information S1.

2.5. Laser-Ablation ICPMS Measurements

In the higher pressure experiments, depletion of Sn in the silicate part of the samples resulted in concentrations below detection limits of EPMA analysis. LA-ICPMS measurements were performed at the University of Brest in order to obtain Sn concentrations in the silicate phases of multianvil experiments. Ablation was conducted using a 193 nm Compex Pro 102 Coherent Laser Ablation System coupled to an Element XR

Table 2
Main Parameters of All Experiments, Average Major and Trace Element Compositions of Metal and Silicate Phases by EPMA and LA-ICPMS and Isotopic Compositions by MC-ICPMS

Experiment	E257	E258	E259	E260	E265	E267	E268	E272	E273
Starting material	A	C	C	A	C	A	B	B	B
Pressure (GPa)	2	2	2	2	2	2	2	2	2
Temperature (K)	1,696	1,696	1,796	1,796	2,296	2,296	1,823	2,296	2,100
Duration (min)	30	30	15	15	1.5	3	15	2	5
Pressure media	Talc-pyrex	Talc-pyrex	Talc-pyrex	Talc-pyrex	$BaCO_3$	$BaCO_3$	Talc-pyrex	$BaCO_3$	$BaCO_3$
Capsule	BN	BN	BN	BN	BN	BN	BN	MgO	MgO
Silicate composition (oxide wt.%)									
n	40	30	25	24	19	6	26	67	71
SiO_2	51.36 ± 0.42	49.96 ± 0.32	50.14 ± 0.26	51.74 ± 0.55	45.58 ± 1.42	46.23 ± 0.43	52.06 ± 0.69	34.54 ± 0.33	33.79 ± 0.24
Al_2O_3	15.87 ± 0.13	15.48 ± 0.04	15.47 ± 0.06	16.05 ± 0.09	14.28 ± 0.30	14.24 ± 0.21	16.12 ± 0.26	8.49 ± 0.44	11.50 ± 0.32
CaO	10.21 ± 0.13	9.97 ± 0.08	9.93 ± 0.04	10.43 ± 0.11	9.36 ± 0.11	9.20 ± 0.10	9.09 ± 0.99	5.69 ± 0.36	8.56 ± 0.45
MgO	8.37 ± 0.05	8.14 ± 0.02	8.05 ± 0.05	8.58 ± 0.03	7.21 ± 0.13	7.03 ± 0.11	8.15 ± 0.08	41.81 ± 0.87	32.94 ± 1.09
FeO	3.99 ± 0.18	4.91 ± 0.14	4.73 ± 0.29	3.59 ± 0.18	4.20 ± 1.14	5.03 ± 0.10	3.50 ± 0.28	5.76 ± 0.16	7.61 ± 0.21
B_2O_3	3.84 ± 0.25	5.56 ± 0.11	5.60 ± 0.14	3.20 ± 0.16	12.99 ± 4.39	10.89 ± 1.69	3.08 ± 0.52	0.09 ± 0.02	0.02 ± 0.01
Na_2O	2.94 ± 0.04	2.75 ± 0.03	2.90 ± 0.03	3.34 ± 0.02	2.80 ± 0.95	2.81 ± 0.08	3.47 ± 0.06	1.77 ± 0.17	2.86 ± 0.20
TiO_2	1.76 ± 0.04	1.72 ± 0.02	1.70 ± 0.02	1.78 ± 0.02	1.48 ± 0.05	1.45 ± 0.06	1.74 ± 0.05	0.98 ± 0.06	1.36 ± 0.06
K_2O	0.68 ± 0.01	0.66 ± 0.01	0.67 ± 0.01	0.72 ± 0.01	0.65 ± 0.10	0.67 ± 0.02	0.66 ± 0.07	0.42 ± 0.04	0.65 ± 0.04
P_2O_5	0.13 ± 0.01	0.13 ± 0.01	0.13 ± 0.003	0.14 ± 0.01	0.05 ± 0.048	0.11 ± 0.01	0.14 ± 0.02	0.13 ± 0.01	0.20 ± 0.01
SnO_2	0.08 ± 0.02	0.06 ± 0.02	0.06 ± 0.02	0.10 ± 0.01	0.08 ± 0.03	0.36 ± 0.01	0.03 ± 0.01	0.10 ± 0.01	0.20 ± 0.01
SO_2	0.01 ± 0.003	0.04 ± 0.01	0.06 ± 0.03	0.01 ± 0.002	0.17 ± 0.08	0.03 ± 0.004	0.01 ± 0.003	0.04 ± 0.002	0.04 ± 0.002
N					0.57 ± 0.89	0.91 ± 0.33	N.D.	N.D.	N.D.
Total	99.23 ± 0.74	99.38 ± 0.25	99.43 ± 0.32	99.67 ± 0.55	99.41 ± 4.76	98.96 ± 1.60	98.05 ± 1.68	99.82 ± 0.08	99.74 ± 0.08
Metal composition (wt.%)									
n	23	31	27	29	22	23	21	31	33
Fe	72.31 ± 0.19	69.76 ± 0.12	69.69 ± 0.09	72.40 ± 0.22	72.10 ± 0.28	73.11 ± 0.17	85.47 ± 0.19	85.01 ± 0.26	85.56 ± 0.18
Sn	23.12 ± 0.17	10.99 ± 0.10	10.45 ± 0.11	23.12 ± 0.23	9.16 ± 0.33	21.87 ± 0.14	11.37 ± 0.14	12.33 ± 0.18	12.14 ± 0.15
P	0.23 ± 0.01	0.15 ± 0.00	0.16 ± 0.01	0.24 ± 0.00	0.24 ± 0.01	0.29 ± 0.02	0.25 ± 0.01	0.15 ± 0.01	0.12 ± 0.00
S	0.22 ± 0.01	16.12 ± 0.14	15.46 ± 0.12	0.24 ± 0.01	14.48 ± 0.32	0.26 ± 0.03	0.24 ± 0.02	0.23 ± 0.02	0.23 ± 0.02
Si	0.03 ± 0.01	0.01 ± 0.001	0.01 ± 0.001	0.04 ± 0.01	0.01 ± 0.001	0.10 ± 0.05	0.09 ± 0.00	0.03 ± 0.01	0.01 ± 0.001
O					0.82 ± 0.50	0.02 ± 0.01	N.D.	0.65 ± 0.06	0.45 ± 0.03
B					0.01 ± 0.01	N.D.	0.04 ± 0.01	N.D.	N.D.
N					0.08 ± 0.07	0.31 ± 0.03	N.D.	N.D.	N.D.
Ti					0.004 ± 0.001	0.01 ± 0.00	0.01 ± 0.00	0.01 ± 0.002	0.005 ± 0.001
Mg								0.07 ± 0.004	0.07 ± 0.001
Total	95.65 ± 0.07	96.86 ± 0.06	95.74 ± 0.08	96.00 ± 0.08	96.39 ± 0.27	95.80 ± 0.08	97.33 ± 0.10	98.28 ± 0.10	98.40 ± 0.06
D_{Sn}	394 ± 79	211 ± 53	209 ± 86	328 ± 21	128 ± 44	86 ± 3	411 ± 128	182 ± 15	91 ± 6
$\log K^D_{Sn}$	1.14 ± 0.09	1.06 ± 0.11	1.03 ± 0.18	1.01 ± 0.04	0.74 ± 0.19	0.56 ± 0.02	1.07 ± 0.14	0.90 ± 0.04	0.73 ± 0.03
ΔIW	−2.92	−2.53	−2.58	−3.01	−2.73	−2.75	−3.09	−2.73	−2.47
nbo/t	0.86	1.02	1.02	0.82	1.67	1.49	0.75	3.11	2.53
Metal and silicate isotopic compositions (‰)									
$\delta^{122/118}Sn_{silicate}$	−0.18 ± 0.01		−0.38 ± 0.03	−0.21 ± 0.01	−0.26 ± 0.01	0.06 ± 0.01	0.09 ± 0.01	0.10 ± 0.02	0.12 ± 0.01
$\delta^{122/118}Sn_{metal}$	0.26 ± 0.02		0.35 ± 0.06	0.18 ± 0.01	0.16 ± 0.02	0.29 ± 0.03	0.20 ± 0.03	0.30 ± 0.04	0.34 ± 0.04
$\Delta^{122/118}Sn_{met-sil}$	0.43 ± 0.02		0.73 ± 0.09	0.38 ± 0.02	0.43 ± 0.03	0.23 ± 0.04	0.10 ± 0.04	0.21 ± 0.06	0.22 ± 0.05

Table 2
Continued

Experiment	E290	E291	E292	E294	E295	E296
Starting material	C	D	B	D	E	E
Pressure (GPa)	2	2	2	2	2	2
Temperature (K)	1,873	2,200	1,950	2,025	2,200	2,293
Duration (min)	10	3	10	8	3	2
Pressure media	Talc-pyrex	$BaCO_3$	$BaCO_3$	$BaCO_3$	$BaCO_3$	$BaCO_3$
Capsule	BN	BN	BN	BN	BN	BN
Silicate composition (oxide wt.%)						
n	40	30	25	24	19	6
SiO_2	49.62 ± 0.47	48.67 ± 1.19	49.35 ± 0.86	48.81 ± 0.54	45.34 ± 0.30	43.70 ± 0.67
Al_2O_3	15.68 ± 0.16	14.59 ± 0.42	14.69 ± 0.31	14.63 ± 0.15	5.29 ± 0.10	5.49 ± 0.13
CaO	9.80 ± 0.09	11.89 ± 0.28	11.99 ± 0.12	11.99 ± 0.11	4.05 ± 0.03	3.96 ± 0.07
MgO	8.11 ± 0.11	8.09 ± 0.26	8.26 ± 0.09	8.15 ± 0.10	34.68 ± 0.29	34.64 ± 0.37
FeO	4.70 ± 0.25	5.15 ± 0.19	4.37 ± 0.43	3.79 ± 0.14	3.00 ± 0.15	3.12 ± 0.20
B_2O_3	3.84 ± 0.25	5.56 ± 0.11	5.60 ± 0.14	3.20 ± 0.16	12.99 ± 4.39	10.89 ± 1.69
Na_2O	3.19 ± 0.41	2.18 ± 0.08	2.18 ± 0.06	2.18 ± 0.12	0.42 ± 0.06	0.41 ± 0.04
TiO_2	1.74 ± 0.09	0.97 ± 0.08	1.03 ± 0.08	0.97 ± 0.07	0.17 ± 0.03	0.17 ± 0.06
K_2O	0.61 ± 0.03	0.17 ± 0.01	0.17 ± 0.01	0.17 ± 0.02	0.03 ± 0.01	0.04 ± 0.01
P_2O_5	0.11 ± 0.03	0.15 ± 0.03	0.13 ± 0.04	0.11 ± 0.04	0.03 ± 0.03	0.02 ± 0.02
SnO_2	0.06 ± 0.02	0.08 ± 0.01	0.05 ± 0.01	0.06 ± 0.01	0.03 ± 0.01	0.04 ± 0.01
SO_2	0.08 ± 0.03	0.03 ± 0.02	0.02 ± 0.02	0.02 ± 0.01	0.01 ± 0.01	0.01 ± 0.01
N_2O	1.05 ± 0.35	2.10 ± 0.85	0.75 ± 0.52	1.55 ± 0.30	3.41 ± 0.62	3.50 ± 1.08
CuO		0.07 ± 0.01		0.04 ± 0.01	0.07 ± 0.01	0.07 ± 0.01
Total	98.05 ± 1.59	97.91 ± 1.68	95.34 ± 2.17	96.06 ± 1.43	106.53 ± 2.27	104.77 ± 1.45
Metal composition (wt.%)						
n	15	12	13	16	15	16
Fe	70.67 ± 0.15	81.00 ± 0.66	84.60 ± 0.51	81.76 ± 0.48	80.10 ± 0.63	80.71 ± 0.41
Sn	10.36 ± 0.14	11.71 ± 0.48	11.68 ± 0.39	10.30 ± 0.51	9.18 ± 0.41	9.57 ± 0.32
P	0.14 ± 0.01	0.13 ± 0.01	0.12 ± 0.01	0.13 ± 0.01	0.01 ± 0.003	0.01 ± 0.002
S	17.19 ± 0.21	0.36 ± 0.07	0.32 ± 0.04	0.36 ± 0.05	0.01 ± 0.002	0.01 ± 0.003
Si	0.02 ± 0.003	0.40 ± 0.02	0.25 ± 0.02	0.38 ± 0.06	0.54 ± 0.12	0.39 ± 0.13
O	0.52 ± 0.05	0.21 ± 0.02	0.14 ± 0.02	0.06 ± 0.01	0.12 ± 0.02	0.08 ± 0.01
Ti	0.03 ± 0.01	0.01 ± 0.002	0.01 ± 0.002	0.01 ± 0.004	0.01 ± 0.002	0.01 ± 0.002
Mg	0.01 ± 0.003	0.01 ± 0.003	0.01 ± 0.004	0.03 ± 0.01	0.01 ± 0.003	0.01 ± 0.003
Cu	0.045 ± 0.011	4.28 ± 0.21	0.05 ± 0.01	2.29 ± 0.09	4.02 ± 0.20	3.55 ± 0.08
Total	98.95 ± 0.11	98.11 ± 0.10	97.17 ± 0.17	96.17 ± 0.58	93.98 ± 0.12	94.30 ± 0.11
D_{Sn}	183 ± 56	192 ± 26	299 ± 39	215 ± 33	470 ± 80	414 ± 73
$\log K^D_{Sn}$	0.99 ± 0.13	0.92 ± 0.06	1.04 ± 0.07	0.84 ± 0.07	0.98 ± 0.11	0.93 ± 0.08
ΔIW	−2.54	−2.72	−2.86	−2.99	−3.38	−3.38
nbo/t	0.85	0.98	0.85	0.93	3.16	3.53

Table 2
Continued

Experiment	E317	E342	E345	H4735	H4950	H4951	H4952	E396	E397
Starting material	F	F	F	G	F	F	G	G	G
Pressure (GPa)	2	2	2	10	12	14	12	2	2
Temperature (K)	1,873	1,773	2,273	2,273	2,273	2,373	2,373	1,873	1,773
Duration (min)	5	15	1	5	5	2	2	5	15
Pressure media	Talc-pyrex	Talc-pyrex	$BaCO_3$	$MgO+Cr_2O_3$	$MgO+Cr_2O_3$	$MgO+Cr_2O_3$	$MgO+Cr_2O_3$	Talc-pyrex	Talc-pyrex
Capsule	MgO	MgO	MgO	MgO SC	MgO SC	MgO SC	MgO SC	MgO	MgO
Silicate composition (oxide wt.%)									
n	21	18	25	30	13	14	10	13	29
SiO_2	40.05 ± 0.46	41.14 ± 0.26	30.15 ± 0.51	37.66 ± 0.20	38.57 ± 0.16	37.99 ± 0.32	36.54 ± 0.54	41.44 ± 1.43	39.79 ± 0.19
Al_2O_3	10.66 ± 1.12	10.00 ± 1.23	8.26 ± 0.15	9.24 ± 0.15	9.10 ± 0.25	10.16 ± 0.17	8.27 ± 0.13	10.06 ± 0.76	12.56 ± 0.31
CaO	8.54 ± 0.96	7.94 ± 1.05	7.60 ± 0.15	8.60 ± 0.18	9.22 ± 0.19	9.26 ± 0.23	8.66 ± 0.28	7.65 ± 0.70	10.15 ± 0.31
MgO	29.35 ± 2.56	27.88 ± 2.97	28.59 ± 0.84	34.31 ± 0.31	35.71 ± 0.36	34.74 ± 0.42	37.06 ± 0.60	24.58 ± 1.02	20.12 ± 0.75
FeO	8.26 ± 0.25	10.11 ± 0.12	11.66 ± 0.24	7.09 ± 0.10	5.67 ± 0.13	5.95 ± 0.09	7.41 ± 0.09	10.64 ± 0.86	13.39 ± 0.10
Na_2O	1.85 ± 0.22	1.53 ± 0.21	1.15 ± 0.03	0.78 ± 0.02	1.18 ± 0.05	1.22 ± 0.04	1.01 ± 0.04	2.06 ± 0.13	1.99 ± 0.05
TiO_2	0.71 ± 0.08	0.68 ± 0.09	0.46 ± 0.01	0.72 ± 0.03	0.70 ± 0.03	0.73 ± 0.03	0.71 ± 0.03	0.69 ± 0.07	0.88 ± 0.03
K_2O	0.20 ± 0.02	0.15 ± 0.02	0.15 ± 0.003	0.16 ± 0.01	0.13 ± 0.01	0.14 ± 0.01	0.09 ± 0.01	0.20 ± 0.02	0.17 ± 0.003
P_2O_5	0.01 ± 0.001	0.02 ± 0.002	0.06 ± 0.003	0.06 ± 0.003	0.01 ± 0.000	0.01 ± 0.001	0.07 ± 0.003	0.07 ± 0.006	0.09 ± 0.001
SO_2	0.01 ± 0.001	0.01 ± 0.001	0.05 ± 0.003	0.12 ± 0.01	0.008 ± 0.001	0.01 ± 0.001	0.55 ± 0.04	0.18 ± 0.02	0.24 ± 0.01
SnO								0.07 ± 0.006	0.08 ± 0.003
Total	99.99 ± 0.31	99.74 ± 0.28	88.61 ± 0.51	99.30 ± 0.17	100.89 ± 0.12	100.76 ± 0.13	101.30 ± 0.26	98.18 ± 0.36	100.08 ± 0.50
Sn (ppm)	268 ± 80	300 ± 136	1,146 ± 226	10,08 ± 100	222 ± 19	188 ± 26	2,106 ± 146		
Metal composition (wt.%)									
n	23	31	27	29	22	23	21	31	33
Fe	31	27	25	28	14	11	15	12	14
Fe	87.58 ± 0.26	86.76 ± 0.64	89.51 ± 0.16	64.91 ± 0.35	80.66 ± 0.61	80.73 ± 0.72	60.63 ± 0.60	62.80 ± 1.26	63.33 ± 0.55
Sn	3.82 ± 0.05	3.86 ± 0.03	3.43 ± 0.06	5.29 ± 0.06	5.08 ± 0.11	4.55 ± 0.05	5.21 ± 0.07	5.33 ± 0.21	5.20 ± 0.13
P	0.08 ± 0.004	0.09 ± 0.004	0.001 ± 0.000	0.01 ± 0.001	0.09 ± 0.004	0.11 ± 0.004	0.010 ± 0.002	0.02 ± 0.004	0.02 ± 0.002
S	0.24 ± 0.01	0.24 ± 0.01	0.10 ± 0.01	16.15 ± 0.14	0.26 ± 0.01	0.29 ± 0.02	19.98 ± 0.26	10.31 ± 0.40	11.08 ± 0.23
Si	0.02 ± 0.002	0.01 ± 0.002	0.01 ± 0.001	0.01 ± 0.002	0.04 ± 0.01	0.02 ± 0.004	0.02 ± 0.001	0.01 ± 0.004	0.03 ± 0.03
O	0.01 ± 0.01	0.16 ± 0.04	N.D.	1.32 ± 0.13	0.19 ± 0.03	0.17 ± 0.05	1.41 ± 0.27	0.42 ± 0.07	0.55 ± 0.05
Ti	N.D.	0.004 ± 0.001	0.003 ± 0.001	N.D.	0.008 ± 0.002	N.D.	N.D.	0.002 ± 0.001	0.003 ± 0.001
Mg	0.14 ± 0.002	0.14 ± 0.002	0.15 ± 0.004	0.10 ± 0.00	0.13 ± 0.004	0.13 ± 0.004	0.08 ± 0.001	0.09 ± 0.007	0.09 ± 0.006
Total	98.74 ± 0.22	99.10 ± 0.55	97.71 ± 0.15	98.25 ± 0.26	98.08 ± 0.50	98.24 ± 0.66	97.26 ± 0.18	92.68 ± 0.49	94.06 ± 0.17
D_{Sn}	159 ± 47	147 ± 67	30 ± 6	53 ± 5	279 ± 24	292 ± 41	25 ± 2	98 ± 10	83 ± 4
$\log K^D_{Sn}$	1.01 ± 0.13	1.07 ± 0.20	0.48 ± 0.09	0.64 ± 0.04	1.09 ± 0.04	1.14 ± 0.06	0.3 ± 0.03	1.06 ± 0.06	1.09 ± 0.02
ΔIW	−2.39	−2.19	−2.01	−2.17	−2.71	−2.66	−2.07	−1.87	−1.65
nbo/t	2.88	2.76	3.64	3.24	3.27	3.23	3.60	2.63	2.60

Table 2
Continued

Experiment	Z1820	Z1821	Z1823	Z1824	Z1825	Z1956	Z1957	Z1959
Starting material	G	F	F	F	G	F	G	F
Pressure (GPa)	7	7	14	18	18	20	20	16
Temperature (K)	1,979	2,023	2,573	2,473	2,473	2,573	2,573	2,473
Duration (min)	10	1	1	4	4	1	1	1
Pressure media	$MgO+Cr_2O_3$	$MgO+Cr_2O_3$	$MgO+Cr_2O_3$	$MgO+Cr_2O_3$	$MgO+Cr_2O_3$	$MgO+Cr_2O_3$	$MgO+Cr_2O_3$	$MgO+Cr_2O_3$
Capsule	MgO SC	MgO SC	MgO SC	MgO SC	MgO SC	MgO SC	MgO SC	MgO SC
Silicate composition (oxide wt.%)								
n	13	19	13	9	22	15	13	15
SiO_2	35.29 ± 0.90	48.54 ± 1.04	39.39 ± 0.55	44.82 ± 0.35	39.16 ± 0.16	39.45 ± 0.68	39.90 ± 0.34	37.78 ± 0.43
Al_2O_3	9.72 ± 1.25	12.07 ± 0.58	9.09 ± 0.29	14.12 ± 0.95	8.83 ± 0.14	9.32 ± 0.07	8.93 ± 0.07	9.73 ± 0.11
CaO	6.96 ± 0.99	12.33 ± 0.41	9.10 ± 0.45	10.32 ± 0.07	9.69 ± 0.10	9.36 ± 0.26	9.48 ± 0.21	8.98 ± 0.24
MgO	35.89 ± 1.86	15.35 ± 0.30	35.61 ± 0.91	23.44 ± 0.37	30.42 ± 0.18	33.36 ± 0.97	31.53 ± 0.51	36.88 ± 0.68
FeO	9.98 ± 0.26	8.45 ± 0.54	5.99 ± 0.12	4.86 ± 0.45	7.79 ± 0.07	6.15 ± 0.14	6.52 ± 0.11	5.93 ± 0.12
Na_2O	0.69 ± 0.11	1.75 ± 0.14	1.16 ± 0.04	1.00 ± 0.16	1.06 ± 0.03	1.34 ± 0.03	1.26 ± 0.03	1.11 ± 0.03
TiO_2	0.70 ± 0.10	0.78 ± 0.08	0.68 ± 0.04	0.77 ± 0.07	0.82 ± 0.03	0.72 ± 0.02	0.67 ± 0.04	0.73 ± 0.02
K_2O	0.22 ± 0.03	0.10 ± 0.02	0.14 ± 0.01	0.11 ± 0.02	0.14 ± 0.01	0.15 ± 0.01	0.12 ± 0.005	0.12 ± 0.01
P_2O_5	0.08 ± 0.01	0.02 ± 0.005	0.01 ± 0.000	0.01 ± 0.001	0.09 ± 0.02	0.01 ± 0.000	0.04 ± 0.002	0.01 ± 0.000
SO_2	0.16 ± 0.02	0.005 ± 0.001	0.006 ± 0.001	0.002 ± 0.001	0.11 ± 0.01	0.01 ± 0.001	0.27 ± 0.01	0.008 ± 0.001
Total	100.10 ± 0.60	100.03 ± 0.98	101.73 ± 0.21	100.22 ± 0.21	99.99 ± 0.26	100.56 ± 0.18	99.99 ± 0.16	101.88 ± 0.11
Sn (ppm)	1,385 ± 65	368 ± 151	272 ± 8	208 ± 20	2497 ± 258	259 ± 72	2,407 ± 415	250 ± 34
Metal composition (wt.%)								
n	10	18	39	33	43	19	16	9
Fe	59.99 ± 1.32	87.00 ± 0.60	78.02 ± 0.50	78.77 ± 0.35	63.29 ± 0.35	78.26 ± 0.82	62.90 ± 0.82	76.38 ± 5.09
Sn	4.65 ± 0.26	4.80 ± 0.11	5.58 ± 0.09	4.92 ± 0.05	6.35 ± 0.19	4.19 ± 0.31	6.60 ± 0.23	4.24 ± 0.36
P	0.001 ± 0.000	0.17 ± 0.04	0.08 ± 0.005	0.06 ± 0.005	0.01 ± 0.001	0.09 ± 0.01	0.03 ± 0.01	0.06 ± 0.01
S	17.90 ± 0.44	0.32 ± 0.05	0.31 ± 0.01	0.23 ± 0.006	15.91 ± 0.22	0.30 ± 0.02	16.73 ± 0.69	0.23 ± 0.02
Si	0.03 ± 0.001	N.D.	0.05 ± 0.01	0.04 ± 0.005	0.04 ± 0.01	0.23 ± 0.06	0.01 ± 0.01	0.04 ± 0.006
O	1.97 ± 0.18	0.19 ± 0.06	1.25 ± 0.14	0.99 ± 0.13	1.55 ± 0.11	0.36 ± 0.07	1.17 ± 0.35	0.38 ± 0.10
Ti	N.D.	N.D.	N.D.	N.D.	N.D.	0.003 ± 0.001	N.D.	N.D.
Mg	0.09 ± 0.003	0.23 ± 0.06	0.18 ± 0.03	0.13 ± 0.01	0.11 ± 0.02	0.12 ± 0.004	0.41 ± 0.33	0.12 ± 0.01
Total	98.17 ± 0.13	99.99 ± 0.68	98.15 ± 0.28	98.03 ± 0.13	98.07 ± 0.18	98.48 ± 0.32	96.85 ± 0.33	98.55 ± 0.43
D_{Sn}	34 ± 3	142 ± 58	247 ± 9	268 ± 25	26 ± 3	197 ± 56	28 ± 5	214 ± 34
$\log K^D_{Sn}$	0.64 ± 0.04	1.00 ± 0.18	1.09 ± 0.02	1.05 ± 0.06	0.38 ± 0.05	0.99 ± 0.13	0.34 ± 0.08	1.01 ± 0.08
ΔIW	−1.80	−2.30	−2.61	−2.76	−2.06	−2.61	−2.22	−2.65
nbo/t	3.51	1.94	3.22	2.24	3.07	3.11	3.03	3.37

Note. Errors correspond to one standard deviation σ.

high-resolution mass spectrometer. Data accuracy is ensured via internal calibrations, using Mg concentrations previously measured by EPMA, and by standard interpolations using glass standards NIST610, NIST612, and NIST614 (see Supporting Information S1).

2.6. Sample Preparation and Dissolution

Metallic and silicate phases stemming from piston cylinder experiments were separated mechanically and crushed. The eventual metallic pieces contaminating the silicate were removed magnetically. Crushed silicates were digested in a 1:3 solution of $HF:HNO_3$. Metals were dissolved in 6 N HCl. The samples in closed

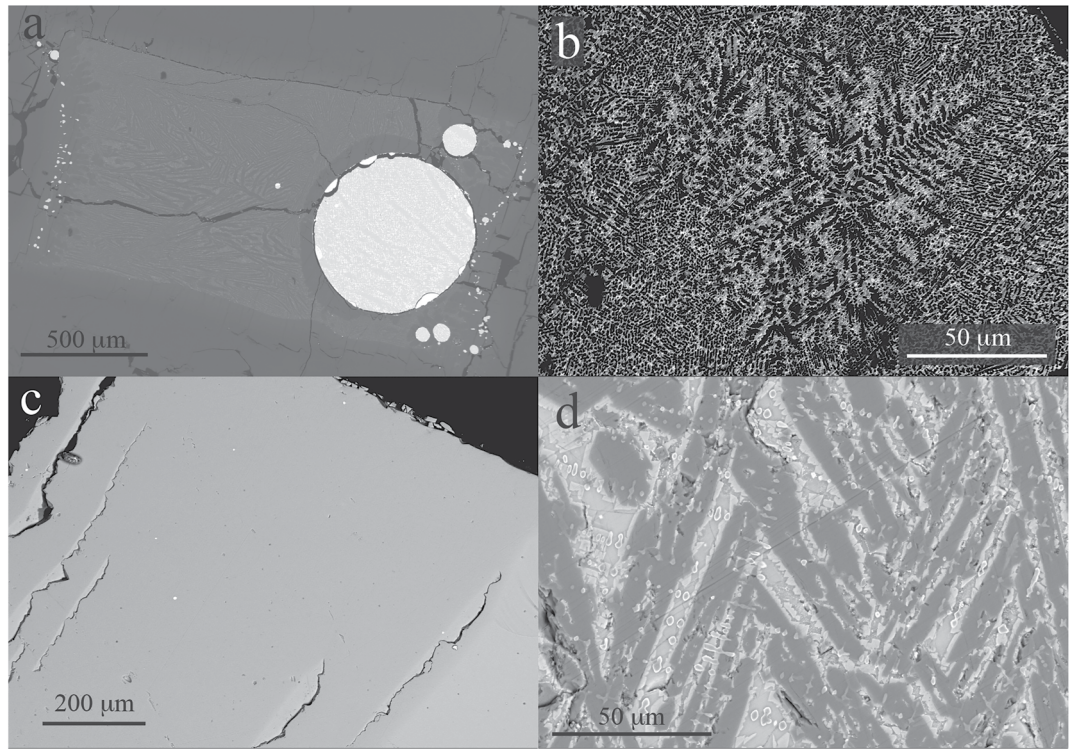


Figure 1. Back-scattered electron images from typical multianvil and piston cylinder run products. (a) Image of H4950 multianvil experiment (12 GPa, 2,273K). The average composition of both phases are measured with 30 μm rasters on the electron microprobe, and a 90 μm beam size for laser ablation in order to homogenize quench textures in the metal and in the silicate that correspond to local chemical heterogeneities. (b) Image of metal phase (piston cylinder, 2 GPa, 1,797 K) showing dendritic quench texture. (c) Image of silicate phase of run 268 (piston cylinder, 2 GPa, 1,823 K) typical of low temperature, boron nitride encapsulated runs showing clean glass with a few ~1 μm metal nuggets. (d) Image of silicate phase of run 272 (piston cylinder, 2 GPa, 2,296 K) showing typical quench textures for high temperature MgO-encapsulated experiments with dendritic olivine crystals and interstitial pyroxenite glass (brighter gray).

Teflon beakers were heated on a hotplate at 100°C. Samples were double-spiked using the method described in Creech, Moynier, and Badullovich (2017) by addition of a ^{117}Sn-^{122}Sn double-spike solution in the sample beaker with the prospect of producing proportions of 39.77% double-spike Sn and 60.23% from the sample.

2.7. Chemical Purification of Sn

Tin was separated from the rest of the sample prior to isotopic analysis to avoid interferences using the ion exchange chromatography technique described in Creech, Moynier, and Badullovich (2017). Biorad columns containing 1 mL of Eichrom TRU resin were used. Tin cuts were then recovered in 10 mL of 0.5 N HNO_3. This chemical process is executed in order to recover a Sn cut containing about 1 μg of Sn. Each Sn cut was then dried and redissolved into 0.5 N HCl for a concentration of ca. 100 ng mL^{-1} for mass spectrometer analysis. The protocol is described in detail in the Supporting Information S1.

2.8. Mass Spectrometry and Data Reduction

Tin isotope measurements were performed using a Neptune Plus MC-ICP-MS (IPGP, Paris) following the method described in Creech, Moynier, and Badullovich (2017). Samples were analyzed one to three times during 412 s (50 cycles), inducing a consumption of 70 ng of Sn per analysis. Cups were configured as to collect ^{116}Sn, ^{117}Sn, ^{118}Sn, ^{119}Sn, ^{120}Sn, ^{121}Sb, ^{122}Sn, ^{123}Sb, and ^{124}Sn. Blanks were <1 ng and two natural samples were measured along with our samples and found to reproduce values published previously (Creech & Moynier, 2019; see Supporting Information S1). All isotope data reduction was performed using Isospike (www.isospike.org; Creech & Paul, 2015), providing results expressed as $\delta^{122/118}$Sn (permil variation with respect to Sn_IPGP standard).

3. Results

3.1. Petrography

In each experiment, the superliquidus temperature allowed the metal to coalesce into a single sphere, measuring about 1 mm in piston cylinder experiments and 500 μm in multianvil experiments (Figure 1a). This sphere was surrounded by the silicate part of the sample, which sometimes contains several other much smaller metal spheres (Figure 1a). All silicate phases were glassy (Figure 1c) except for the higher temperature MgO encapsulated experiments, in which MgO diffusion led to crystallisation of olivine and pyroxene (Figure 1d). The metallic phases have quench textures (Figure 1b). Those primary petrographic observations indicate that the starting material was fully molten in all experiments, allowing equilibrium achievement within a few minutes at most (Thibault & Walter, 1995). Si-doped experiments present several immiscible phases in the metal part and some metal contamination in the silicate as micro- and nano-nuggets and were therefore discarded from this study.

3.2. Elemental Compositions

All elemental data from EPMA and LA-ICPMS are presented in Table 2. The MgO content of the silicate phases of the experiments, from 6.5 to 41.8 wt.%, is a function of experimental temperature since the MgO introduction from the capsule to the sample is favored at higher temperatures. The MgO content is inferior to 30 wt.% in the silicate of boron nitride encapsulated experiments. The SiO_2 content ranges from 30.1 to 52 wt.%. Sn concentration varies from 100 to 4,000 μg g^{-1}.

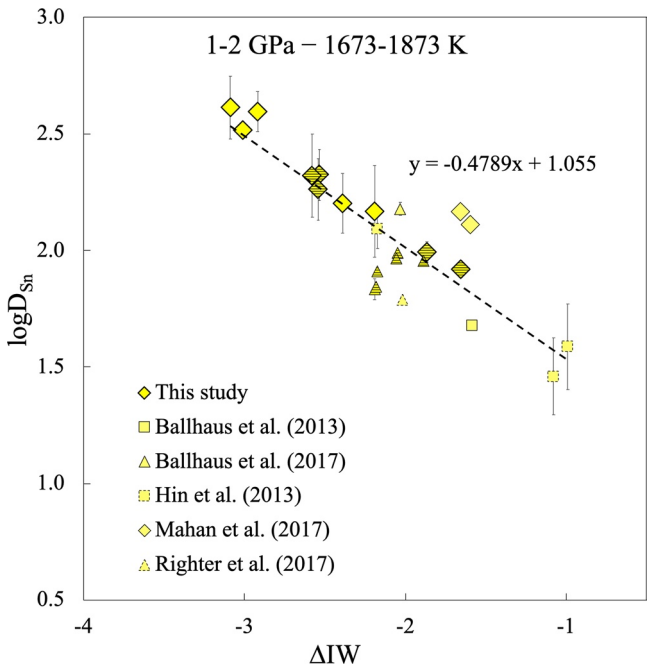


Figure 2. Partition coefficient $\log D_{Sn}$ as a function of oxygen fugacity ΔIW calculated relatively to iron-wüstite (Equation 1) for all experiments between 1 and 2 GPa and 1,673–1,873 K of this study and data compiled from literature (Ballhaus et al., 2013, 2017; Hin et al., 2013; Mahan et al., 2017; Righter et al., 2017). Errors correspond to one standard deviation (σ) and were propagated from EPMA and LA-ICPMS measurements of this study and from literature. The variation in partition coefficient over a significant interval of fO_2 allows accurate determination of the valence state of Sn. In fact, it can be demonstrated that $\log D_{Sn}$ is a function of $n/4 \log fO_2$ (Siebert et al., 2011). With the slope of the regression line shown on this figure equal to 0.5, we demonstrate that Sn has a valence of 2+ over a range of more than 2 log units. Experiments containing more that 1 mol% of S in the metal part are represented with a horizontal lines pattern. They were included in this figure because in this study we find that S has no effect on Sn partitioning at 1–2 GPa.

The metallic phases of the experiments are dominated by Fe. The S content varies from 0 to 17.4 wt.%. Tin concentration ranges from 3.3 to 23 wt.%.

Both silicate and metallic phases are compositionally homogeneous at the scale of EPMA analyses. Oxygen fugacity is calculated as follows, relative to the iron-wüstite (IW) buffer:

$$\Delta IW = 2 \cdot \log \frac{X_{FeO}^{silicate}}{X_{Fe}^{metal}} \quad (1)$$

ΔIW varies from −3.38 to −1.6 in the experiments (Table 2).

3.3. Metal–Silicate Sn Partitioning

Tin metal–silicate partitioning can be written as a chemical exchange redox reaction:

$$SnO_{n/2}^{silicate} + \frac{n}{2} Fe^{metal} = \frac{n}{2} FeO^{silicate} + Sn^{metal} \quad (2)$$

where n is the valence of Sn. Valence of Sn was determined for the range of fO_2 in our experiments and is demonstrated in Figure 2, where Sn partitioning is plotted as a function of fO_2. The slope of the regression line presented here corresponds to $n/4$ (Siebert et al., 2011) and is shown to be 0.5 in this study. Therefore, this allows precise determination of a valence state of 2+ for Sn in the experiments of this study and associated literature data. This is in agreement with recent study by Vogel et al. (2018) explicitly focused on the valence state of moderately volatile elements in silicate melts. However, it is noted that this result is in contradiction with the Sn^{4+} valence state used in Righter et al. (2019) and based on different datasets acquired at very different experimental conditions (e.g., Capobianco et al., 1999). Further XANES study is needed to fully resolve the Sn valence state in silicate melts. As a 2+ valence state is currently the most harmonious, herein this value is used for calculations and modeling.

The metal–silicate partition coefficient corresponds to the ratio of molar fractions:

$$D_{Sn} = \frac{X_{Sn}^{metal}}{X_{SnO}^{silicate}} \quad (3)$$

The equilibrium constant associated with the redox reaction (Equation 2) is:

$$K = \frac{\left(a_{FeO}^{silicate}\right) \cdot \left(a_{Sn}^{metal}\right)}{\left(a_{SnO}^{silicate}\right) \cdot \left(a_{Fe}^{metal}\right)} \quad (4)$$

where a is the activity of the different components, and $a = \gamma_i X_i$, where γ_i is the activity coefficient and X_i is the mole fraction:

$$\log K = \log \frac{\left(X_{FeO}^{silicate}\right) \cdot \left(X_{Sn}^{metal}\right)}{\left(X_{SnO}^{silicate}\right) \cdot \left(X_{Fe}^{metal}\right)} + \log\left(\frac{\gamma_{Sn}^{metal}}{\gamma_{Fe}^{metal}}\right) + \log\left(\frac{\gamma_{FeO}^{silicate}}{\gamma_{SnO}^{silicate}}\right) \quad (5)$$

The influence of silicate melt composition is represented by the last term of this equation. In our experiments, two different silicate compositions were used, MORB and peridotite, and no difference in partitioning was found between experiments ran at similar conditions. To further investigate this effect, the nbo/t parameter, corresponding to molar ratio of non-bridging oxygens per tetrahedrally coordinated cation, was calculated (Table 2), and found to have no effect on Sn partitioning for groups of experiments that share similar conditions. Furthermore, it is demonstrated that elements with low valence state are very little affected by the structure and composition of the melt (Siebert et al., 2011). For Sn, having a valence state of 2+ and showing no effect in partitioning for the different silicate compositions tested, the effect of the silicate composition is not further investigated in this study and is considered negligible. The logK is simplified as follows:

$$\log K = \log \frac{\left(X_{FeO}^{silicate}\right) \cdot \left(X_{Sn}^{metal}\right)}{\left(X_{SnO}^{silicate}\right) \cdot \left(X_{Fe}^{metal}\right)} + \log\left(\frac{\gamma_{Sn}^{metal}}{\gamma_{Fe}^{metal}}\right) \quad (6)$$

$$\log K = \log K_{Sn}^{D} + \log\left(\frac{\gamma_{Sn}^{metal}}{\gamma_{Fe}^{metal}}\right) \quad (7)$$

The equilibrium constant $\log K_{Sn}^{D}$ is used to compare the partitioning of different experiments with different oxygen fugacities. The $\log K_{Sn}^{D}$ is equal to the partition coefficient of Sn divided by that of Fe, allowing to normalize the partitioning with fO_2:

$$\log K_{Sn}^{D} = \log\left(\frac{X_{Sn}^{metal}}{X_{SnO_2}^{silicate}} \cdot \frac{X_{FeO}^{silicate}}{X_{Fe}^{metal}}\right) = \log \frac{D_{Sn}}{D_{Fe}} \quad (8)$$

The partitioning represented by the exchange coefficient $\log K_{Sn}^{D}$ is presented in Figure 3 as a function of reciprocal temperature. The $\log K_{Sn}^{D}$ varies from 0.41 to 1.40 in this study. No difference in $\log K_{Sn}^{D}$ was detected between the BN encapsulated experiments and those in MgO for similar pressure and temperature conditions. The group of experiments from 1 to 3 GPa, represented in yellow, contains experiments doped with 2 and 8 wt.% of Sn and three experiments from Mahan et al. (2017) are doped with 16 wt.% Sn, which appears not to affect the Sn partitioning. This group of low pressure experiments shows a slight dependence of the partitioning on temperature, which results in Sn behaving less siderophile at higher temperatures, as reported in recent study by Steenstra, Berndt, et al. (2020), although they observe a stronger temperature effect. The higher pressure experiments present enhanced Sn siderophility, which indicates a marked effect of pressure on Sn partitioning. Amongst the low pressure experiments (1–3 GPa), no difference in Sn partitioning is

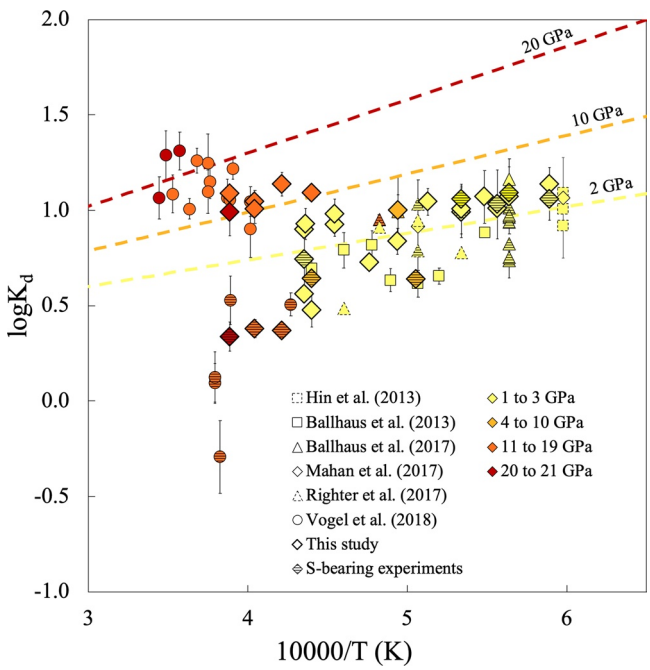


Figure 3. Exchange coefficient $\log K_D$ plotted as a function of reciprocal temperature for all experiments of this study and data compiled from literature (Ballhaus et al., 2013, 2017; Hin et al., 2013; Mahan et al., 2017; Righter et al., 2017; Vogel et al., 2018). Errors correspond to one standard deviation (σ) and were propagated from EPMA and LA-ICPMS measurements of this study and from literature. Experiments containing more that 1 mol% of S in the metal part are represented with a horizontal lines pattern. All experiments are color-coded according to their pressure: 1–3 GPa in yellow, 4–10 GPa in orange, 10–19 GPa in light red, >19 GPa in dark red. Multilinear regression fits are also displayed at IW-2 in several conditions: 2, 10, and 20 GPa with no S in the metal. Sn partitioning is affected by temperature, Sn becoming less siderophile as the temperature increases. Pressure has a positive and strong effect on partition coefficients. S also presents a notable effect on $\log K_D$ which tends to lower the partitioning as the S content of the metal phase increases above 4 GPa.

observed between S-bearing experiments and experiments from which the metal is devoid of S. On the other hand, experiments from 4 to 21 GPa display a strong decrease of Sn partitioning in S-bearing experiments compared to experiments of similar pressures which are devoid of S in their metal. The presence of a significant amount of S in the metal makes Sn less siderophile above 4 GPa.

3.4. Isotopic Compositions

All isotopic data collected via MC-ICPMS analysis are presented in Table 2. Results are expressed using delta-notation as $\delta^{122/118}$Sn which represents the difference in per mil in the ^{122}Sn/^{118}Sn ratio of the sample relative to the standard Sn_IPGP. In the silicate phases of the experiments, $\delta^{122/118}$Sn ranges from −0.38 to 0.12, and from 0.16 to 0.35 in the metal fraction. Metal is found to be enriched in Sn heavier isotopes in all experiments. The bulk $\delta^{122/118}$Sn of each experiment was measured by MC-ICPMS and found equal to 0.22 ± 0.03 (2sd, $n = 8$) which is identical within error to the average calculated bulk $\delta^{122/118}$Sn = 0.25 ± 0.14 (2sd) computed from metal and silicate isotopic compositions, indicating negligible Sn loss during the experiments.

3.5. Metal–Silicate Sn Isotopic Fractionation

The isotopic fractionation is calculated for each experiment as follows:

$$\Delta^{122/118}\mathrm{Sn}_{\mathrm{met-sil}} = \delta^{122/118}\mathrm{Sn}_{\mathrm{met}} - \delta^{122/118}\mathrm{Sn}_{\mathrm{sil}} \quad (9)$$

Sn isotopic fractionation $\Delta^{122/118}\mathrm{Sn}_{\mathrm{met-sil}}$ is positive for all experiments and ranges from 0.10 to 0.73.

4. Discussion

4.1. Equilibrium Conditions

Elemental and isotopic equilibrium between metal and silicate is crucial for accurate characterization of Sn's behavior at such conditions. Petrographic observation of the experimental run products of this study shows no compositional zoning in either metal or silicate (Figure 1). The time duration of experiments was chosen according to the temperature of the run and in agreement with previous studies (Corgne et al., 2008; Mahan et al., 2017; Siebert et al., 2011) that report time series experiments at superliquidus conditions and evidence equilibrium achievement after few tens of seconds.

4.2. Sn Metal–Silicate Partitioning and Earth Accretion

4.2.1. Thermodynamic Parameterization

The thermodynamic formalism shown above (Equation 6) can be restructured as follows:

$$\log \mathrm{K_D} = a + b \cdot \frac{1}{\mathrm{T}} + c \cdot \frac{\mathrm{P}}{\mathrm{T}} - \log\left(\frac{\gamma_{\mathrm{Sn}}^{\mathrm{metal}}}{\gamma_{\mathrm{Fe}}^{\mathrm{metal}}}\right) \quad (10)$$

K_D values were calculated using measurements performed with the electron microprobe and LA-ICPMS for each experiments. The values of a, b, and c were computed using the least-squares multivariate linear regression using results from experiments with no S in the metal from this study and from previous studies (Ballhaus et al., 2013, 2017; Hin et al., 2013; Mahan et al., 2017; Righter et al., 2017; Vogel et al., 2018, see Supporting Information S1):

$$\log \mathrm{K} = 0.18 \pm 0.20 + 1236 \pm 363 \cdot \frac{1}{\mathrm{T}} + 77.9 \pm 13 \cdot \frac{\mathrm{P}}{\mathrm{T}} \quad (11)$$

The regression lines shown in Figure 3 were computed using the calculated regression parameters. S-bearing experiments were used to calculate the interaction parameters. The activity coefficients $\gamma_{\mathrm{Sn}}^{\mathrm{metal}}$ and $\gamma_{\mathrm{Fe}}^{\mathrm{metal}}$ were computed using the interaction parameter approach developed by Ma (2001):

$$\log \mathrm{K_D} = \log\frac{\mathrm{D_{Sn}}}{\mathrm{D_{Fe}}} = a + b \cdot \frac{1}{\mathrm{T}} + c \cdot \frac{\mathrm{P}}{\mathrm{T}} - \log\gamma_{\mathrm{Sn}}^{0} + \varepsilon_{\mathrm{Sn}}^{\mathrm{Sn}} \cdot \log\left(1 - \mathrm{X_{Sn}}\right) + \varepsilon_{\mathrm{Sn}}^{\mathrm{S}} \cdot \log\left(1 - \mathrm{X_S}\right) \quad (12)$$

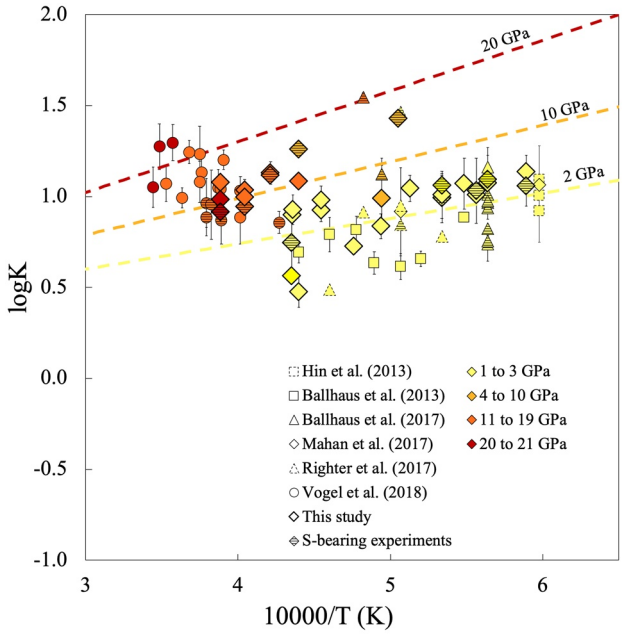


Figure 4. LogK determined experimentally as a function of reciprocal temperature for all experiments of this study and data compiled from literature (Ballhaus et al., 2013, 2017; Hin et al., 2013; Mahan et al., 2017; Righter et al., 2017; Vogel et al., 2018). Errors correspond to one standard deviation σ and were propagated from EPMA and LA-ICPMS measurements of this study and from literature. Experiments containing more that 1 mol% of S in the metal are represented with a horizontal lines pattern. All experiments are color-coded according to their pressure: 1–3 GPa in yellow, 4–10 GPa in orange, 11–19 GPa in light red, >19 GPa in dark red. Multilinear regression fits are also displayed at IW-2 in several conditions: 2, 10, and 20 GPa with no S in the metal. LogK being defined as $a + b\cdot\frac{1}{T} + c\cdot\frac{P}{T}$, this figure displays the effect of pressure and temperature alone on Sn partitioning between metal and silicate.

where ε^{i}_{Sn} represents interaction parameters and γ^{0}_{Sn} the activity coefficient of Sn. ε^{S}_{Sn} is the interaction parameter representing the effect of the presence of S on Sn activity. ε^{S}_{Sn} is a function of pressure, temperature and S and Sn concentrations. ε^{Sn}_{Sn} and γ^{0}_{Sn} are equal to −0.29 and 0.95 respectively at 1873 K (J.S.P.S., 1988). ε^{S}_{Sn} was fitted to the experimental data set and found to be equal to 5.8 ± 0.38. Our results indicate that ε^{S}_{Sn} is pressure-dependent, in good agreement with other studies detecting an effect of pressure on interaction coefficients ε^{S}_{M} (Kubik et al., 2021; Wang et al., 2016) and ε^{Si}_{M} (Steenstra, Seegers, et al., 2020) for several siderophile elements. Such pressure effect could be explained by structural transitions of liquid metal at pressures above 5 GPa (e.g., Morard et al., 2007; Siebert et al., 2004; Sanloup et al., 2011) or in the silicate (e.g., Lee et al., 2003). Values of logK for all experiments of the data set are shown in Figure 4. This expression of Sn metal–silicate partitioning only displays the effect of pressure and temperature. When using this interaction correction, S-bearing experiments show similar partitioning to experiments that are devoid of this element.

4.2.2. Core Formation Models

Core formation models are used in order to recalculate the partition coefficient of an element at each incremental step of Earth's accretion (Rubie et al., 2015; Rudge et al., 2010; Wade & Wood, 2005). The final coefficient obtained can then be compared to the observed partition coefficient determined for the Earth. This method allows to test multiple accretion scenarios and assess whether those scenarios can realistically explain the observed concentration of an element in the Earth's mantle.

In this study, the experimentally calculated regression parameters were used to model the evolution of Sn partitioning during several scenarios of Earth's accretion using the following equation:

$$\log D_{Sn} = a + b\cdot\frac{1}{T} + c\cdot\frac{P}{T} + \varepsilon^{S0}_{Sn}\cdot\frac{1873}{T}\cdot\log\left(1 - X_S\right) - \log\left(\frac{X_{FeO}}{X_{Fe}}\right) \quad (13)$$

ε^{Sn}_{Sn} and γ^{0}_{Sn} found in Equation 12 simplify here because Sn is very dilute in the materials considered in our models. In those models, the differentiation occurs in a continuous way over Earth's accretion (Wade & Wood, 2005). The pressure and temperature conditions, which are those of the base of a deep magma ocean, evolve over the course of the accretion (see Supporting Information S1). Several degrees of equilibration between core and mantle were tested. The parameter k represents the fraction of the core of the accreted embryo that equilibrates with the mantle of the proto-Earth. A full equilibration is modeled with k equal to 1, and lowering k allows to model a partial equilibration. The formalism proposed by Deguen et al. (2014) was used to model the efficiency of the equilibration with more precision with parameter ε which represents the equilibration efficiency based on k and other considerations such as the mass of silicate that is dragged toward the core along with the metal when metal segregation occurs, preventing full equilibration. All full equilibration models presented here use $k = 1$ and all partial equilibration models use an ε with $k = 0.5$. Results of homogeneous core formation models are presented in Figure 5a. The model computed in the case of partial equilibration shows a lower final partition coefficient than the one using only a k parameter to quantify the equilibration efficiency, but those two models cannot be reconciled with the Sn partitioning coefficient of Earth, which is estimated at 8.5 ± 5 (see Supporting Information S1) based on the apparent depletion of Sn relative to the canonical volatility curve (Lodders, 2003; Palme et al., 2013).

A heterogeneous accretion scenario was also considered in order to investigate the effect on Sn partitioning of a delivery of all the volatiles in the later part of the main phases of Earth's accretion as proposed in previous studies (Braukmüller et al., 2019; Kubik et al., 2021; Suer et al., 2017) (Figure 5b). The computation of the delivery of Earth's volatile elements, including Sn and S, in the last 10%–20% of accretion generated a final Sn partitioning that is significantly lower than in the homogeneous accretion scenario, mainly due

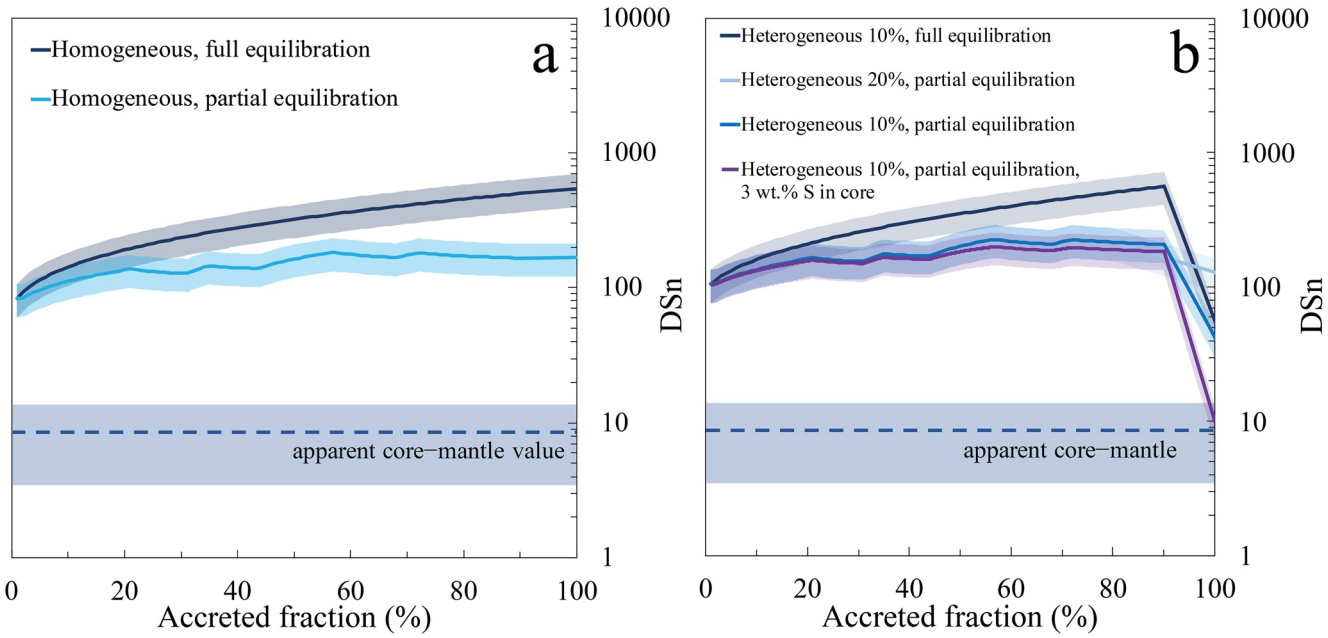


Figure 5. Evolution of D_{Sn} during Earth's accretion computed from core formation models with full and partial equilibration and 1.8 wt.% S in the core of the final Earth. (a) Tin partitioning with continuous and homogeneous core formation models with full and partial equilibration. For partial equilibration, ε was computed with $k = 0.5$. The final D_{Sn} displayed for Earth are respectively 544 ± 145 and 167 ± 45. The use of an ε is lowering significantly the partitioning of Sn, but the final values are too high to be compared to the observed Sn partitioning on Earth (8.56 ± 5.07), shown as a dotted line on the figure. (b) Tin partitioning as a function of the percentage of accreted Earth computed from continuous heterogeneous core formation models in which all the Sn and S were brought in the last 20% or in the last 10% of Earth's accretion in order to simulate a late accretion stage. The obtained final D_{Sn} are lower than in the scenario presented in (a): 128 ± 34 for the light blue curve which represents a 20% late accretion stage with partial equilibration, 55 ± 15 for the dark blue curve corresponding to a 10% late accretion stage with full equilibration, 42 ± 11 for the blue curve which shows a 10% late accretion stage with partial equilibration, using an ε with $k = 0.5$, and 9.9 ± 2.6 for the purple curve representing a model identical to the previous one with 3 wt.% of S in the core. The partitioning is still distinct from the observed value shown in dotted line (8.56 ± 5.07) except when more S is brought into the core. In those models we used a succession of planetesimals of different sizes to be accreted at each steps: 0.1, 1, 10, and 20 wt.% of the Earth's total mass. In calculations considering a partial equilibration, the partitioning coefficients are sensitive to the size of the accreted embryos which is why we observe variations on the curve at stages where there is a change of size of accreted bodies.

to the effect of a higher concentration of S which makes Sn less siderophile, combined with a partial equilibration of the impactors' cores with the Earth's mantle. With a scenario of volatile delivery in the last 20% of accretion, the final D_{Sn} is still an order of magnitude higher than the observed partitioning. When the volatile content delivery of the Earth was concentrated in the last 10% of accretion, lower partition coefficients were obtained (56 ± 14 with full equilibration and 42 ± 11 in the case of partial equilibration). The reason for this is that most of the S and Sn budgets of the Earth are concentrated in one last embryo in the model which therefore has a high S core content which helps put a lot of Sn in the mantle of this embryo. When accreted, this 10 wt.% embryo's mantle equilibrates with the planet's mantle, lowering the final D_{Sn} of the planet. Since the S content in the core of the Earth was found to have such a large influence on Sn partitioning in the Earth, this parameter was varied in Figure 6 from 1.8 wt.%—which is the value proposed in literature from cosmochemical estimates (e.g., McDonough, 2003)—to 4 wt.%, computed with a volatile delivery in the last 10% of the accretion using an equilibration efficiency parameter ε with $k = 0.5$. We find that with 2.5–3.5 wt.% of S in the core, the observed Sn partitioning coefficient for this accretion scenario matches the observed value (Figures 5b and 6). Although there is no consensus on the exact S content of the core, the 2.5–3.5 wt.% found in this study are in good agreement within error with cosmochemical estimates (McDonough, 2003), recent partitioning studies at comparable P and T conditions (Mahan, Siebert, Blanchard, Borensztajn, et al., 2018; Suer et al., 2017), and mineral physics studies (Badro et al., 2014; Morard et al., 2013). Other light elements are thought to be present in significant abundances in the Earth's core such as O, C, and Si (e.g., Allègre et al., 1995; Ringwood, 1977) and could have an effect on Sn partitioning. The effect of Si is not included in our parametrization for the reasons mentioned above, but it should be noted that the interaction parameter predicted by Righter

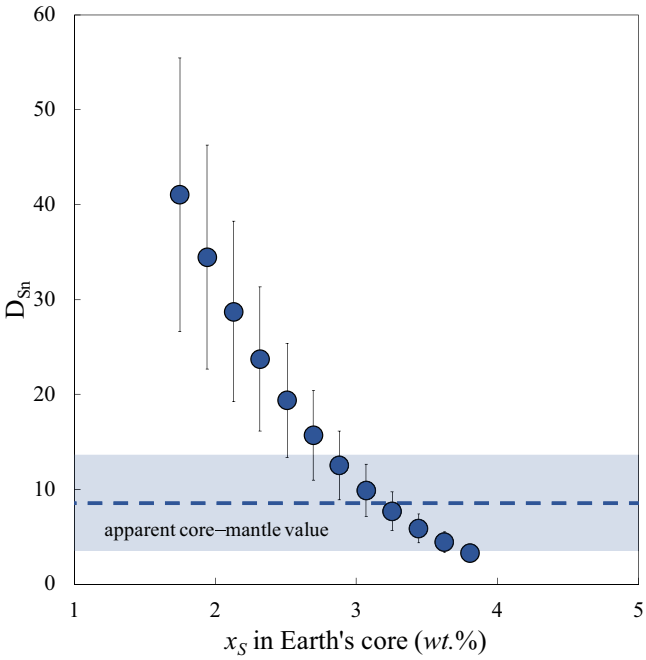


Figure 6. Heterogeneous partial equilibration core formation models. The final D_{Sn} is plotted for a range of different S concentrations that are forced into the Earth's core. D_{Sn} is computed in the case of a late accretion of Sn and S in the last 10% of Earth's formation, using an ε and with $k = 0.5$. In this calculation the bulk S content of the accreted embryos are entered as input and the X_S in the cores of the embryos and Earth are computed using multilinear regression equation from Rose-Weston et al. (2009) which describes the experimentally determined behavior of S in a metal–silicate equilibrium. It shows that if there is 3 wt.% of S in the Earth's core, the apparent partitioning of Sn, plotted as a blue dotted line, can be perfectly reconciled with the computed partitioning inferred from experimental data.

et al. (2019) would influence the parameterization and further models and conclusions of this study.

4.2.3. Tin Metal–Silicate Isotopic Fractionation

Equilibrium mass dependent fractionation of isotopes decreases as a function of the reciprocal square of temperature (Urey, 1947):

$$\Delta^{122/118}\mathrm{Sn}_{\mathrm{met-sil}} = a \cdot \frac{1}{\mathrm{T}^2} \quad (14)$$

Using the data set of this study displayed on Figure 7, parameter a is found to be equal to $1.18 \cdot 10^6 \pm 0.05 \cdot 10^6$ K^{-2}. S-bearing experiments show higher Sn isotopic fractionation than the rest of the data set and are therefore excluded for parameterization considering their unrealistic S content compared to natural systems. More S-bearing experiments are needed to properly parameterize this effect. No difference in isotopic fractionation is detected between experiments performed in BN capsules and those in MgO capsules.

A significant Sn metal–silicate isotopic fractionation was measured from the experimental data set of this study. This result seems to be in disagreement with the rather small difference between the β-factors of pure α-Sn and SnO-bearing silicates reported from recent nuclear resonant inelastic X-ray scattering (NRIXS) measurements (Roskosz et al., 2020). This argues against a measurable Sn isotopic fractionation during core formation. However, such conclusions were reached on samples that are not geochemically relevant (i.e., quenched glasses, pure Sn solid metal) at room pressure and further NRIXS measurements need to be carried out to confirm this potential discrepancy with the present work. The parameterization of this fractionation with temperature variation indicates that at conditions relevant for Earth core–mantle equilibrium (~3000 K), the resultant mantle could be isotopically lighter than the core by 150–200 ± 17 ppm per amu. Although a lot of isotopic systems predict an enrichment of the mantle in heavy isotopes (e.g., Mo: Hin et al., 2013; Si: Hin et al., 2014), it is not unusual to detect a light isotope enrichment in the silicate part (e.g., S: Labidi et al., 2016; Fe: Elardo & Shahar, 2017; Shahar et al., 2015; Ni: Guignard et al., 2020). Recent measurements of Sn isotopic compositions of chondrites by Creech and Moynier (2019) show an overlap between the carbonaceous chondrites composition and that of the primitive mantle measured by Badullovich et al. (2017). This overlap could be the result of two scenarios: (a) The Sn budget of the Earth did not equilibrate with the core, either through the addition of an unequilibrated late veneer, and/or a low rate of partial equilibration between core and mantle; or (b) the temperature during core–mantle differentiation was higher than 4000 K, preventing detectable Sn isotopic fractionation, as suggested by recent work by Olson and Sharp (2019). In this second case, the Sn isotopic signature of the BSE would match the signature of its building blocks, which would then only match that of carbonaceous chondrites (and not enstatite or ordinary chondrites, see Figure 8), in agreement with other cosmochemical observables (Braukmüller et al., 2019; Marty, 2012; O'Neill, 1991).

The experimentally parameterized Sn isotopic fractionation at metal–silicate equilibrium was used as input in an isotopic core formation model in order to test different accretion scenarios, where ordinary, enstatite and carbonaceous chondrites were considered as potential sources for the Earth's volatiles (Figure 8). The conditions of the models match those of the elemental core formation models discussed in the previous section. During metal–silicate equilibration, the metal is preferentially enriched in the heavier isotopes of Sn whereas the silicate is enriched in Sn lighter isotopes. In the computed models, the Sn isotopic composition of one of the three types of chondrites was used as the bulk Sn isotopic composition of the Earth (ordinary: −0.29 ± 0.44‰, enstatite: 0.12 ± 0.28‰ and carbonaceous: 0.47 ± 0.12‰, Creech & Moynier, 2019). The mantle and core isotopic compositions were then calculated both in the case of a homogeneous accretion and an heterogeneous accretion where the volatiles were brought in the last 10% of Earth's accreted mass.

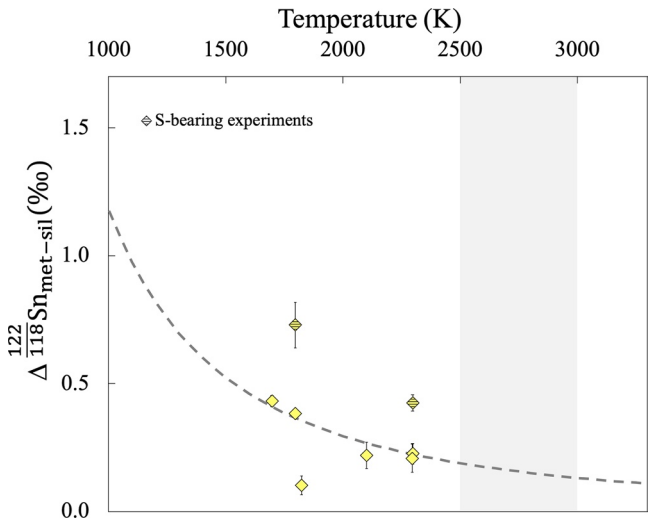


Figure 7. Sn isotope fractionation between metal and silicate from a selection of piston cylinder experiments at 2 GPa as a function of the equilibrium temperature of those experiments. This fractionation is a function of $1/T^2$ (Urey, 1947) as represented by the gray dashed regression. A fractionation between 0.10 and 0.73‰ is observed. S-bearing experiments, represented with a horizontal lines pattern, seem to present a higher fractionation of Sn isotopes between metal and silicate. The gray zone corresponds to temperatures that are relevant to the conditions of core–mantle differentiation in a deep magma ocean on Earth. The interpolation of the regression based on experimental data at such temperatures shows that isotopic fractionation could be observed at Earth's differentiation conditions.

After core–mantle equilibration, the computed isotopic composition was shifted toward lighter values for the mantle compared to the bulk, as expected (Figure 8). The ordinary and enstatite chondrites, of which the average Sn isotopic composition is significantly lighter than the BSE, would produce computed mantle values for Sn isotopes that are even lighter, from −0.60 ± 0.05‰ to −0.08 ± 0.04‰, which are incompatible with the BSE (0.49 ± 0.11‰, Badullovich et al., 2017). On the other hand, results for carbonaceous chondrites isotopic core formation models show good agreement with Sn isotopic composition of the BSE. The dispersion of Sn isotopic compositions within this group of chondrites is displayed on Figure 8. Our computed Sn isotopic BSE composition in the case of heterogeneous accretion, which is 0.37 ± 0.04‰, plots within error of the BSE isotopic composition. The observed BSE Sn isotopic composition could be explained by the same scenario as the observed Sn abundance in the BSE without the need to invoke other processes (i.e., volatilization processes). In this scenario, carbonaceous chondrite-like material appears to be the most likely source of volatile elements on Earth according to our Sn isotope data set. It should be noted that a different and isotopically lighter BSE estimate was proposed by Wang et al. (2018) based on a peridotite sample ($\delta^{122/118}$Sn = 0.27 ± 0.06‰ relative to Sn_IPGP). The use of this lighter estimate would not modify the results of this study, but would in fact strengthen its conclusions. If the S effect observed in the experimental data is confirmed by future studies, the quantification of this effect during Earth's accretion, whether by considering the S content of the core or by modeling sulphide segregation, would increase the Sn core–mantle fractionation and strengthen our conclusions for a late volatile accretion and/or high temperature of core formation (above 4,000 K) and carbonaceous chondrite source material. Wang et al. (2019) propose an estimate of the Bulk Silicate Moon (BSM) of 0.03 ± 0.02‰ ($\delta^{122/118}$Sn relative to Sn_IPGP) which is significantly lighter than the BSE (0.49 ± 0.11‰). Although the Moon and the Earth share common episodes of their accretion history—namely the giant impact stage—the Moon is clearly volatile depleted compared to the Earth most likely because of volatilization processes (Boyce et al., 2015; Kato et al., 2015; Pringle et al., 2014; Pringle & Moynier, 2017; Sharp et al., 2010; Wang & Jacobsen, 2016) or core formation (Steenstra et al., 2016). The light Sn isotopic signature of the BSM is not fully consistent with volatile loss and could be explained by mixing processes between the protolunar disk and the Earth as proposed by Wang et al. (2019), and, as our data suggest, lunar core formation may also have left the silicate fraction of the Moon enriched in the lighter isotopes. The contribution of core formation in establishing the light isotope signature of the BSM is also in agreement with the Moon core formation temperature estimated at 2,300 K by other studies such as Steenstra et al. (2016). According to our experimental data, core formation at such temperature would produce a Sn isotope fractionation of 0.06‰/amu. It should be noted that Sn isotopic measurements being very scarce, more studies reporting additional isotopic data would be much beneficial to further discuss these topics.

4.2.4. Core Formation and Earth's Accretion

A scenario in which the volatile delivery occurs in the last part of the main phases of Earth's accretion is in agreement with numerous other studies. This last stage could be associated to a sulfur-rich iron liquid that forms by sulphide saturation and segregates into the core (referred to as the Hadean matte; Rubie et al., 2016). While our study does not necessitate this added complexity, it does not negate its possibility either. Several studies show volatile elements metal–silicate equilibrium data that cannot be reconciled with the observed abundances in the case of a homogeneous accretion scenario. In particular, Suer et al. (2017), Mahan, Siebert, Blanchard, Badro, et al. (2018) and Mahan, Siebert, Blanchard, Borensztajn, et al. (2018) report sulfur, zinc and copper metal–silicate diamond anvil cell experiments at conditions relevant to Earth's core formation (46–91 GPa), and are able to reconcile their data with the observed S,

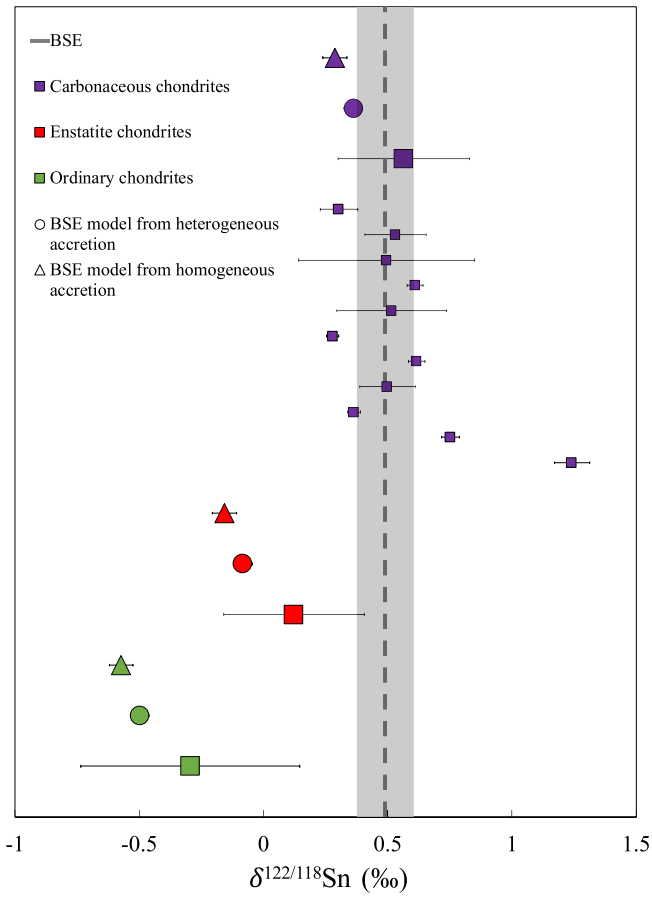


Figure 8. Isotopic compositions of core formation models computed for different types of possible building materials compared to the bulk silicate Earth (BSE) value (Badullovich et al., 2017) in dashed line with uncertainty in gray. Average isotopic compositions of carbonaceous chondrites (purple), enstatite chondrites (red) and ordinary chondrites (green) from Creech and Moynier (2019) are plotted as large squares displaying the standard deviation between single meteorites measurements. Individual measurements of carbonaceous chondrites are represented as small purple squares. Multiple isotopic core formation models were computed using each of the average chondrites $\delta^{122/118}$Sn as the isotopic composition of Earth's building blocks. For each chondrite type, a homogeneous accretion model with an ε and $k = 0.5$ was calculated and represented as a triangle. A heterogeneous model where all the volatiles were brought in the last 10% of Earth's accretion, considering an ε value and $k = 0.5$, is represented as a circle. Error bars of the models correspond to the propagation of uncertainty on the regression parameter. The isotopic composition of carbonaceous chondrites overlap with that of the BSE. The modeled $\delta^{122/118}$Sn of the BSE are lower than the $\delta^{122/118}$Sn from the chosen building block because the heavier isotopes of Sn tend to go preferentially in the core. Models detailing carbonaceous chondrite isotopic compositions generate models that are closer to the BSE than for other potential source materials. Moreover, individual Sn isotopic measurements of carbonaceous chondrites (small purple squares) overlap with that of the BSE (with notable dispersion), and both overlap with our heterogeneous model. Based on this evidence, carbonaceous chondrite-like material appears to be the best potential source of volatile elements on Earth.

Zn and Cu contents of the present-day mantle with a volatile delivery in the last part of the main phases of the Earth's accretion, a scenario also supported by Ballhaus et al. (2017), Huang et al. (2021) and Kubik et al. (2021). This accretion pathway is not only backed by metal–silicate studies, but isotopic measurements of Pd-Ag and noble gases as well as Mo and Ru anomalies (Budde et al., 2019; Hopp et al., 2020; Marty, 2012; Schonbachler et al., 2010) show that terrestrial isotopic data can only be explained by a heterogeneous accretion scenario. A study on halogens abundances and ratios (Clay et al., 2017) corroborates late-stage accretion of volatile-rich planetesimals. Numerical simulations put spatial constraints on this mechanism showing that the source of volatiles on Earth was probably an influx of material from the outer solar system which was delivered late in the planet's growth (Lichtenberg et al., 2021; Morbidelli et al., 2012; Raymond et al., 2006). O'Brien et al. (2018) and Schiller et al. (2018) also state that this late delivery is composed of material originated from beyond the snow line and chemically similar to carbonaceous chondrites.

Carbonaceous chondrites appear to have contributed to terrestrial planet building blocks, and are the most likely source of volatiles on Earth according to numerous studies (e.g., O'Neill, 1991; Schonbachler et al., 2010). Recent work on S, Se, and Te measurements (Braukmüller et al., 2019) shows that the most volatile elements are unfractionated from one another in Earth and chondrites, creating a volatile element plateau (or "hockey-stick" pattern). Braukmüller et al. (2019) propose a scenario of delivery of volatiles under the form of 10–15 wt.% of CI-like material before core formation ceased (potentially as a giant, Moon-forming impact), in view of the depletion of siderophile and chalcophile volatile elements relative to the observed plateau.

Moreover, though the systematic linkage of water and other volatile species is debatable, the highly volatile elements (e.g., H, N, Kr, and Xe) further support volatile delivery via carbonaceous chondrite-like material. For example the D/H ratios of carbonaceous chondrites are consistent with the bulk Earth value (Alexander et al., 2012; Sarafian et al., 2017). The coupled similarity in H and N isotopic compositions between CI chondrites and the bulk Earth also advocates for a carbonaceous chondritic source for volatile elements in the Earth's mantle (Marty, 2012). For heavy noble gases, isotope data obtained on mantle-derived samples also show a chondritic affinity for these noble gases in the silicate portion of Earth (Holland et al., 2009; Péron & Moreira, 2018), although some studies suggest that there could be multiple noble gas reservoirs in the deep mantle (Tucker & Mukhopadhyay, 2014). However, recent study by Piani et al. (2020) focusing on H and N isotopes suggests that Earth's water could originate from enstatite chondrite-like material.

Lastly, recent modeling results of large impact dynamics strongly support the notion that most or all volatiles are retained during Earth's accretion (Lock & Stewart, 2017; Daly & Schultz, 2018). A similar message is delivered by Siebert et al. (2018) regarding the chondritic Mn/Na ratio observed on Earth, favoring incomplete accretion in the solar nebula over syn- and post-accretion volatilization processes to explain the volatile depletion. Taken together, these observations converge toward retainment of most or all inherited volatiles during the entire accretionary process and volatile signatures established from nebular processes.

Assuming that Earth's Sn budget and isotopic signature have been inherited from its source material (Creech & Moynier, 2019), our results show that any difference in Sn isotope composition and abundances between the BSE and potential building blocks (e.g., carbonaceous chondrites) is largely a consequence of the process of core formation.

5. Conclusions

Thirty piston cylinder and multianvil press experiments have been performed to characterize the metal–silicate behavior of Sn at high pressure and high temperature. A double approach was used in which both Sn elemental partitioning and Sn isotopic fractionation were measured at metal–silicate equilibrium. Subsequent parameterization and core formation models show that pressure has a notable positive effect on Sn partitioning that makes the relatively high Sn content of the Earth's mantle largely incompatible with a scenario of homogeneous accretion and associated differentiation. The observed Sn concentration in the BSE can be reconciled with our experimental data only in an accretionary scenario where most of the volatile elements budget was delivered during the last 10% of the main phases of Earth's formation. Moreover, around 3 wt.% of S in the core are needed to sufficiently lower the modeled partitioning in order to match the observed Sn abundance. Tin isotopes are found to be fractionated at metal–silicate equilibrium, such that the mantle ought to become enriched in the lighter isotopes during core formation. If no other process fractionated Sn isotopes, the bulk Earth should then be heavier than the bulk silicate Earth value. For ordinary and enstatite chondrite types, previous work has established that the averages of available Sn isotopic compositions are significantly lighter than the BSE estimate, whereas carbonaceous chondrites provide a plausible match. Our isotope data therefore suggest that the most likely source of Earth's volatiles is carbonaceous chondrite-like material.

Acknowledgments
The authors thank JGR Editor Stephen W. Parman, Associate Editor John Lassiter and two anonymous reviewers for their detailed and constructive comments. The authors acknowledge the financial support of the UnivEarthS Labex program at Sorbonne Paris Cité (ANR-10-LABX-0023 and ANR-11-IDEX-0005-02). Part of the work was supported by IPGP multidisciplinary program PARI, by Région Île-de-France SESAME Grants no. 12015908, EX047016 and the IdEx Université de Paris grant, ANR-18-IDEX-0001 and the DIM ACAV+. The authors thank Stephan Borensztajn for support during SEM observations. The authors acknowledge and thank the DFG Core Facility Program at Bayerisches Geoinstitut. We thank Michel Fialin and Nicolas Rividi for technical support at the EPMA platform CAMPARIS. The authors thank Bleuenn Guéguen for technical support during LA-ICPMS measurements at IUEM, University of Brest. The authors also thank Nicolas Wehr for technical support and advice in high-pressure laboratory of IPGP. The authors thank Pascale Louvat for technical support and advice in the MC-ICPMS laboratory. JS thanks the financial support of the French National Research Agency (ANR Project VolTerre, grant no. ANR-14-CE33-0017-01). FM acknowledges funding from the European Research Council under the H2020 framework program/ERC grant agreement #637503 (Pristine), and the ANR through a chaire d'excellence Sorbonne Paris Cité.

Data Availability Statement

All the data are available in Table 2 and in the following repository: https://data.mendeley.com/datasets/5zxjmr5r5j/1.

References

Albarède, F. (2009). Volatile accretion history of the terrestrial planets and dynamic implications. *Nature*, *461*, 1227–1233. https://doi.org/10.1038/nature08477

Albarède, F., Ballhaus, C., Blichert-Toft, J., Lee, C. T., Marty, B., Moynier, F., & Yin, Q. Z. (2013). Asteroidal impacts and the origin of terrestrial and lunar volatiles. *Icarus*, *222*, 44–52. https://doi.org/10.1016/j.icarus.2012.10.026

Alexander, C. M. O. D., Bowden, R., Fogel, M. L., Howard, K. T., Herd, C. D. K., & Nittler, L. R. (2012). The provenances of asteroids, and their contributions to the volatile inventories of the terrestrial planets. *Science*, *337*, 721–723. https://doi.org/10.1126/science.1223474

Allègre, C. J., Poirier, P. J., Humler, E., & Hofmann, A. W. (1995). The chemical composition of the Earth. *Earth and Planetary Science Letters*, *134*, 515–526. https://doi.org/10.1016/0012-821x(95)00123-t

Badro, J., Cote, A. S., & Brodholt, J. P. (2014). A seismologically consistent compositional model of Earth's core. *Proceedings of the National Academy of Sciences*, *111*, 7542–7545. https://doi.org/10.1073/pnas.1316708111

Badullovich, N., Moynier, F., Creech, J., Teng, F.-Z., & Sossi, P. A. (2017). Tin isotopic fractionation during igneous differentiation and Earth's mantle composition. *Geochemical Perspectives Letters*, *5*, 24–28. https://doi.org/10.7185/geochemlet.1741

Ballhaus, C., Fonseca, R. O. C., Münker, C., Rohrbach, A., Nagel, T., Speelmanns, I. M., et al. (2017). The great sulfur depletion of Earth's mantle is not a signature of mantle–core equilibration. *Contributions to Mineralogy and Petrology*, *172*, 68. https://doi.org/10.1007/s00410-017-1388-3

Ballhaus, C., Laurenz, V., Münker, C., Fonseca, R. O. C., Albarède, F., Rohrbach, A., et al. (2013). The U/Pb ratio of the Earth's mantle-A signature of late volatile addition. *Earth and Planetary Science Letters*, *362*, 237–245. https://doi.org/10.1016/j.epsl.2012.11.049

Blanchard, I., Badro, J., Siebert, J., & Ryerson, F. J. (2015). Composition of the core from gallium metal–silicate partitioning experiments. *Earth and Planetary Science Letters*, *427*, 191–201. https://doi.org/10.1016/j.epsl.2015.06.063

Bloom, H., Lodders, K., Chen, H., Zhao, C., Tian, Z., Koefoed, P., et al. (2020). Potassium isotope compositions of carbonaceous and ordinary chondrites: Implications on the origin of volatile depletion in the early solar system. *Geochimica et Cosmochimica Acta*, *277*, 111–131. https://doi.org/10.1016/j.gca.2020.03.018

Bourdon, B., Roskosz, M., & Hin, R. C. (2018). Isotope tracers of core formation. *Earth-Science Reviews*, *181*, 61–81. https://doi.org/10.1016/j.earscirev.2018.04.006

Boyce, J. W., Treiman, A. H., Guan, Y., Ma, C., Eiler, J. M., Gross, J., et al. (2015). The chlorine isotope fingerprint of tsshe lunar magma ocean. *Science Advances*, *1*, 2–10. https://doi.org/10.1126/sciadv.1500380

Braukmüller, N., Wombacher, F., Funk, C., & Münker, C. (2019). Earth's volatile element depletion pattern inherited from a carbonaceous chondrite-like source. *Nature Geoscience*, *12*, 564–568. https://doi.org/10.1038/s41561-019-0375-x

Budde, G., Burkhardt, C., & Kleine, T. (2019). Molybdenum isotopic evidence for the late accretion of outer Solar System material to Earth. *Nature Astronomy*, *3*, 736–741. https://doi.org/10.1038/s41550-019-0779-y

Burkhardt, C., Hin, R. C., Kleine, T., & Bourdon, B. (2014). Evidence for Mo isotope fractionation in the solar nebula and during planetary differentiation. *Earth and Planetary Science Letters*, *391*, 201–211. https://doi.org/10.1016/j.epsl.2014.01.037

Capobianco, C. J., Drake, M. J., & De'Aro, J. (1999). Siderophile geochemistry of Ga, Ge, and Sn: Cationic oxidation states in silicate melts and the effect of composition in iron-nickel alloys. *Geochimica et Cosmochimica Acta*, *63*, 2667–2677. https://doi.org/10.1016/s0016-7037(99)00085-x

Clay, P. L., Burgess, R., Busemann, H., Ruzié-Hamilton, L., Joachim, B., Day, J. M. D., & Ballentine, C. J. (2017). Halogens in chondritic meteorites and terrestrial accretion. *Nature*, *551*, 614–618. https://doi.org/10.1038/nature24625

Corgne, A., Keshav, S., Wood, B. J., McDonough, W. F., & Fei, Y. (2008). Metal-silicate partitioning and constraints on core composition and oxygen fugacity during Earth accretion. *Geochimica et Cosmochimica Acta*, *72*, 574–589. https://doi.org/10.1016/j.gca.2007.10.006

Creech, J. B., Baker, J. A., Handler, M. R., Lorand, J.-P., Storey, M., Wainwright, A. N., et al. (2017). Late accretion history of the terrestrial planets inferred from platinum stable isotopes. *Geochemical Perspectives Letters*, *3*, 94–104. https://doi.org/10.7185/geochemlet.1710

Creech, J. B., & Moynier, F. (2019). Tin and zinc stable isotope characterisation of chondrites and implications for early Solar System evolution. *Chemical Geology*, *511*, 81–90. https://doi.org/10.1016/j.chemgeo.2019.02.028

Creech, J. B., Moynier, F., & Badullovich, N. (2017). Tin stable isotope analysis of geological materials by double-spike MC-ICPMS. *Chemical Geology*, *457*, 61–67. https://doi.org/10.1016/j.chemgeo.2017.03.013

Creech, J. B., Moynier, F., & Koeberl, C. (2019). Volatile loss under a diffusion-limited regime in tektites: Evidence from tin stable isotopes. *Chemical Geology*, *528*, 119279. https://doi.org/10.1016/j.chemgeo.2019.119279

Creech, J. B., & Paul, B. (2015). IsoSpike: Improved double-spike inversion software. *Geostandards and Geoanalytical Research*, *39*, 7–15. https://doi.org/10.1111/j.1751-908x.2014.00276.x

Daly, R. T., & Schultz, P. H. (2018). The delivery of water by impacts from planetary accretion to present. *Science Advances*, *4*, 2632. https://doi.org/10.1126/sciadv.aar2632

Deguen, R., Landeau, M., & Olson, P. (2014). Turbulent metal-silicate mixing, fragmentation, and equilibration in magma oceans. *Earth and Planetary Science Letters*, *391*, 274–287. https://doi.org/10.1016/j.epsl.2014.02.007

Elardo, S. M., & Shahar, A. (2017). Non-chondritic iron isotope ratios in planetary mantles as a result of core formation. *Nature Geoscience*, *10*, 317–321. https://doi.org/10.1038/ngeo2896

Guignard, J., Quitté, G., Méheut, M., Toplis, M. J., Poitrasson, F., Connetable, D., & Roskosz, M. (2020). Nickel isotope fractionation during metal-silicate differentiation of planetesimals: Experimental petrology and *ab initio* calculations. *Geochimica et Cosmochimica Acta*, *269*, 238–256. https://doi.org/10.1016/j.gca.2019.10.028

Hin, R. C., Burkhardt, C., Schmidt, M. W., Bourdon, B., & Kleine, T. (2013). Experimental evidence for Mo isotope fractionation between metal and silicate liquids. *Earth and Planetary Science Letters*, *379*, 38–48. https://doi.org/10.1016/j.epsl.2013.08.003

Hin, R. C., Coath, C. D., Carter, P. J., Nimmo, F., Lai, Y. J., Pogge von Strandmann, P. A. E., et al. (2017). Magnesium isotope evidence that accretional vapour loss shapes planetary compositions. *Nature*, *549*, 511–515. https://doi.org/10.1038/nature23899

Hin, R. C., Fitoussi, C., Schmidt, M. W., & Bourdon, B. (2014). Experimental determination of the Si isotope fractionation factor between liquid metal and liquid silicate. *Earth and Planetary Science Letters*, *387*, 55–66. https://doi.org/10.1016/j.epsl.2013.11.016

Holland, G., Cassidy, M., & Ballentine, C. (2009). Meteorite Kr in Earth's mantle. *Science*, *326*, 1522–1525. https://doi.org/10.1126/science.1179518

Hopp, T., Budde, G., & Kleine, T. (2020). Heterogeneous accretion of Earth inferred from Mo-Ru isotope systematics. *Earth and Planetary Science Letters*, *534*, 116065. https://doi.org/10.1016/j.epsl.2020.116065

Huang, D., Siebert, J., & Badro, J. (2021). High pressure partitioning behavior of Mo and W and late sulfur delivery during Earth's core formation. *Geochimica et Cosmochimica Acta*, *310*. https://doi.org/10.1016/j.gca.2021.06.031

Humayun, M., & Clayton, R. N. (1995). Potassium isotope cosmochemistry: Genetic implications of volatile element depletion. *Geochimica et Cosmochimica Acta*, *59*, 2131–2148. https://doi.org/10.1016/0016-7037(95)00132-8

J.S.P.S. (1988). The Japan Society for the Promotion of Science. The nineteenth committee for steelmaking. In. *The steelmaking sourcebook. Revised*. New York: Gordon & Breach Science Publishers Ltd.

Kato, C., Moynier, F., Valdes, M. C., Dhaliwal, J. K., & Day, J. M. D. (2015). Extensive volatile loss during formation and differentiation of the Moon. *Nature Communications*, *6*, 1–4. https://doi.org/10.1038/ncomms8617

Kubik, E., Siebert, J., Blanchard, I., Agranier, A., Mahan, B., & Moynier, F. (2021). Earth's volatile accretion as told by Cd, Bi, Sb and Tl core–mantle distribution. *Geochimica et Cosmochimica Acta*, *306*, 263–280.

Labidi, J., Shahar, A., Le Losq, C., Hillgren, V. J., Mysen, B. O., & Farquhar, J. (2016). Experimentally determined sulfur isotope fractionation between metal and silicate and implications for planetary differentiation. *Geochimica et Cosmochimica Acta*, *175*, 181–194. https://doi.org/10.1016/j.gca.2015.12.001

Lee, S. K., Fei, Y., Cody, G. D., & Mysen, B. O. (2003). Order and disorder in sodium silicate glasses and melts at 10 GPa. *Geophysical Research Letters*, *30*, 1845. https://doi.org/10.1029/2003gl017735

Lichtenberg, T., Drazkowska, J., Schönbachler, M., Golabek, G. J., & Hands, T. O. (2021). Bifurcation of planetary building blocks during Solar System formation. *Science*, *371*, 365–370. https://doi.org/10.1126/science.abb3091

Lock, S. J., & Stewart, S. T. (2017). The structure of terrestrial bodies: Impact heating, corotation limits, and synestias. *Journal of Geophysical Research: Planets*, *122*, 950–982. https://doi.org/10.1002/2016je005239

Lodders, K. (2003). Solar System abundances and condensation temperatures of the elements. *The Astrophysical Journal*, *591*, 1220–1247. https://doi.org/10.1086/375492

Luck, J. M., Othman, D. B., & Albarède, F. (2005). Zn and Cu isotopic variations in chondrites and iron meteorites: Early solar nebula reservoirs and parent-body processes. *Geochimica et Cosmochimica Acta*, *69*, 5351–5363. https://doi.org/10.1016/j.gca.2005.06.018

Ma, Z. (2001). Thermodynamic description for concentrated metallic solutions using interaction parameters. *Metallurgical and Materials Transactions B*, *32*, 87–103. https://doi.org/10.1007/s11663-001-0011-0

Mahan, B., Siebert, J., Blanchard, I., Badro, J., Kubik, E., Sossi, P., & Moynier, F. (2018). Investigating Earth's formation history through copper and sulfur metal-silicate partitioning during core-mantle differentiation. *Journal of Geophysical Earth: Solid Earth*, *123*, 8349–8363. https://doi.org/10.1029/2018jb015991

Mahan, B., Siebert, J., Blanchard, I., Borensztajn, S., Badro, J., & Moynier, F. (2018). Constraining compositional proxies for Earth's accretion and core formation through high pressure and high temperature Zn and S metal-silicate partitioning. *Geochimica et Cosmochimica Acta*, *235*, 21–40. https://doi.org/10.1016/j.gca.2018.04.032

Mahan, B., Siebert, J., Pringle, E. A., & Moynier, F. (2017). Elemental partitioning and isotopic fractionation of Zn between metal and silicate and geochemical estimation of the S content of the Earth's core. *Geochimica et Cosmochimica Acta*, *196*, 252–270. https://doi.org/10.1016/j.gca.2016.09.013

Marty, B. (2012). The origins and concentrations of water, carbon, nitrogen and noble gases on Earth. *Earth and Planetary Science Letters*, *313–314*, 56–66. https://doi.org/10.1016/j.epsl.2011.10.040

McDonough, W. F. (2003). Compositional model for the Earth's core. In Carlson, R. W. (Ed.), *Treatise on geochemistry* (Vol. 2, pp. 547–568). Oxford: Elsevier-Pergamon. https://doi.org/10.1016/b0-08-043751-6/02015-6

Morard, G., Sanloup, C., Fiquet, G., Mezouar, M., Rey, N., Poloni, R., & Beck, P. (2007). Structure of eutectic Fe-FeS melts to pressures up to 17 GPa: Implications for planetary cores. *Earth and Planetary Science Letters*, *263*, 128–139. https://doi.org/10.1016/j.epsl.2007.09.009

Morard, G., Siebert, J., Andrault, D., Guignot, N., Garbarino, G., Guyot, F., & Antonangeli, D. (2013). The Earth's core composition from high pressure density measurements of liquid iron alloys. *Earth and Planetary Science Letters*, *373*, 169–178. https://doi.org/10.1016/j.epsl.2013.04.040

Morbidelli, A., Lunine, J. I., O'Brien, D. P., Raymond, S. N., & Walsh, K. J. (2012). Building terrestrial planets. *Annual Review of Earth and Planetary Sciences*, *40*, 251–275. https://doi.org/10.1146/annurev-earth-042711-105319

Nebel, O., Mezger, K., & van Westrenen, W. (2011). Rubidium isotopes in primitive chondrites: Constraints on Earth's volatile element depletion and lead isotope evolution. *Earth and Planetary Science Letters*, *305*, 309–316. https://doi.org/10.1016/j.epsl.2011.03.009

Nie, N. X., & Dauphas, N. (2019). Vapor drainage in the protolunar disk as the cause for the depletion in volatile elements of the Moon. *The Astrophysical Journal Letters*, *884*, L48. https://doi.org/10.3847/2041-8213/ab4a16

Norris, C. A., & Wood, B. J. (2017). Earth's volatile contents established by melting and vaporization. *Nature*, *549*, 507–510. https://doi.org/10.1038/nature23645

O'Brien, D. P., Izidoro, A., Jacobson, S. A., Raymond, S. N., & Rubie, D. C. (2018). The delivery of water during terrestrial planet formation. *Space Science Reviews*, *214*, 47.

Olson, P. L., & Sharp, Z. D. (2019). Nebular atmosphere to magma ocean: A model for volatile capture during Earth accretion. *Physics of the Earth and Planetary Interiors*, *294*, 106294. https://doi.org/10.1016/j.pepi.2019.106294

O'Neill, H. S. C. (1991). The origin of the moon and the early history of the earth-A chemical model. Part 1: The moon. *Geochimica et Cosmochimica Acta*, *55*, 1135–1157. https://doi.org/10.1007/bf00058999

O'Neill, H. S. C., & Palme, H. (2008). Collisional erosion and the non-chondritic composition of the terrestrial planets. *Philosophical Transactions of the Royal Society A Mathematical, Physical and Engineering Sciences*, *366*, 4205–4238.

Palme, H., Lodders, K., & Jones, A. (2013). Solar System abundances of the elements. In Davis, A. M. (Ed.), *Treatise on geochemistry* (2nd ed., Vol. 2, pp. 15–36). Oxford: Elsevier-Pergamon.

Palme, H., & O'Neill, H. (2013). Cosmochemical estimates of mantle composition. In Davis, A. M. (Ed.), *Treatise on geochemistry* (2nd ed., Vol. 2, pp. 149–211). Oxford: Elsevier-Pergamon.

Péron, S., & Moreira, M. (2018). Onset of volatile recycling into the mantle determined by xenon anomalies. *Geochemical Perspectives Letters*, *9*, 21–25. https://doi.org/10.7185/geochemlet.1833

Piani, L., Marrocchi, Y., Rigaudier, T., Vacher, L. G., Thomassin, D., & Marty, B. (2020). Earth's water may have been inherited from material similar to enstatite chondrite meteorites. *Science*, *369*, 1110–1113. https://doi.org/10.1126/science.aba1948

Pringle, E. A., & Moynier, F. (2017). Rubidium isotopic composition of the Earth, meteorites, and the Moon: Evidence for the origin of volatile loss during planetary accretion. *Earth and Planetary Science Letters*, *473*, 62–70. https://doi.org/10.1016/j.epsl.2017.05.033

Pringle, E. A., Moynier, F., Beck, P., Paniello, R., & Hezel, D. C. (2017). The origin of volatile element depletion in early solar system material: Clues from Zn isotopes in chondrules. *Earth and Planetary Science Letters*, *468*, 62–71. https://doi.org/10.1016/j.epsl.2017.04.002

Pringle, E. A., Moynier, F., Savage, P. S., Badro, J., & Barrat, J.-A. (2014). Silicon isotopes in angrites and volatile loss in planetesimals. *Proceedings of the National Academy of Sciences*, *111*, 17029–17032. https://doi.org/10.1073/pnas.1418889111

Raymond, S. N., Quinn, T., & Lunine, J. I. (2006). High-resolution simulations of the final assembly of Earth-like planets I. Terrestrial accretion and dynamics. *Icarus*, *183*, 265–282. https://doi.org/10.1016/j.icarus.2006.03.011

Righter, K., & Drake, M. J. (2000). Metal/silicate equilibrium in the early earth-new constraints from the volatile moderately siderophile elements Ga, Cu, P, and Sn. *Geochimica et Cosmochimica Acta*, *64*, 3581–3597. https://doi.org/10.1016/s0016-7037(00)00466-x

Righter, K., Pando, K., Marin, N., Ross, D. K., Righter, M., Danielson, L., et al. (2017). Volatile element signatures in the mantles of Earth, Moon, and Mars: Core formation fingerprints from Bi, Cd, In, and Sn. *Meteoritics & Planetary Sciences*, *22*, 1–16. https://doi.org/10.1016/j.gca.2016.10.045

Righter, K., Pando, K., Ross, D. K., Righter, M., & Lapen, T. J. (2019). Effect of silicon on activity coefficients of Bi, Cd, Sn, and Ag in liquid Fe-Si, and implications for differentiation and core formation. *Meteoritics & Planetary Sciences*, *54*, 1379–1394. https://doi.org/10.1111/maps.13285

Righter, K., Pando, K. M., Danielson, L., & Lee, C. T. (2010). Partitioning of Mo, P and other siderophile elements (Cu, Ga, Sn, Ni, Co, Cr, Mn, V, and W) between metal and silicate melt as a function of temperature and silicate melt composition. *Earth and Planetary Science Letters*, *291*, 1–9. https://doi.org/10.1016/j.epsl.2009.12.018

Ringwood, A. E. (1977). Composition of the core and implications for origin of the Earth. *Geochemical Journal*, *11*, 111–135. https://doi.org/10.2343/geochemj.11.111

Rose-Weston, L., Brenan, J. M., Fei, Y., Secco, R. A., & Frost, D. J. (2009). Effect of pressure, temperature, and oxygen fugacity on the metal-silicate partitioning of Te, Se, and S: Implications for earth differentiation. *Geochimica et Cosmochimica Acta*, *73*, 4598–4615. https://doi.org/10.1016/j.gca.2009.04.028

Roskosz, M., Amet, Q., Fitoussi, C., Dauphas, N., Bourdon, B., Tissandier, L., et al. (2020). Redox and structural controls on tin isotopic fractionations among magmas. *Geochimica et Cosmochimica Acta*, *268*, 42–55. https://doi.org/10.1016/j.gca.2019.09.036

Rubie, D. C., Frost, D. J., Mann, U., Asahara, Y., Nimmo, F., Tsuno, K., et al. (2011). Heterogeneous accretion, composition and core-mantle differentiation of the Earth. *Earth and Planetary Science Letters*, *301*, 31–42. https://doi.org/10.1016/j.epsl.2010.11.030

Rubie, D. C., Jacobson, S. A., Morbidelli, A., O'Brien, D. P., Young, E. D., de Vries, J., et al. (2015). Accretion and differentiation of the terrestrial planets with implications for the compositions of early-formed Solar System bodies and accretion of water. *Icarus*, *248*, 89–108. https://doi.org/10.1016/j.icarus.2014.10.015

Rubie, D. C., Laurenz, V., Jacobson, S. A., Morbidelli, A., Palme, H., Vogel, A. K., & Frost, D. J. (2016). Highly siderophile elements were stripped from Earth's mantle by iron sulphide segregation. *Science*, *353*, 1141–1144. https://doi.org/10.1126/science.aaf6919

Rudge, J. F., Kleine, T., & Bourdon, B. (2010). Broad bounds on Earths accretion and core formation constrained by geochemical models. *Nature Geoscience*, *3*, 439–443. https://doi.org/10.1038/ngeo872

Sanloup, C., van Westrenen, W., Dasgupta, R., Maynard-Casely, H., & Perillat, J.-P. (2011). Compressibility change in iron-rich melt and implications for core formation models. *Earth and Planetary Science Letters*, *306*, 118–122. https://doi.org/10.1016/j.epsl.2011.03.039

Sarafian, A. R., Hauri, E. H., McCubbin, F. M., Lapen, T. J., Berger, E. L., Nielsen, S. G., et al. (2017). Early accretion of water and volatile elements to the inner Solar System: Evidence from angrites. *Philosophical Transactions of the Royal Society A Mathematical, Physical and Engineering Sciences*, *375*(2094). https://doi.org/10.1098/rsta.2016.0209

Savage, P. S., Moynier, F., Chen, H., Shofner, G., Siebert, J., Badro, J., & Puchtel, I. S. (2015). Copper isotope evidence for large-scale sulphide fractionation during Earth's differentiation. *Geochemical Perspectives Letters*, *1*, 53–64. https://doi.org/10.7185/geochemlet.1506

Schiller, M., Bizzarro, M., & Fernandes, V. A. (2018). Isotopic evolution of the protoplanetary disk and the building blocks of Earth and the Moon. *Nature*, *555*, 501–510. https://doi.org/10.1038/nature25990

Schonbachler, M., Carlson, R. W., Horan, M. F., Mock, T. D., & Hauri, E. H. (2010). Heterogeneous accretion and the moderately volatile element budget of Earth. *Science*, *328*, 884–887. https://doi.org/10.1126/science.1186239

Shahar, A., Hillgren, V. J., Horan, M. F., Mesa-Garcia, J., Kaufman, L. A., & Mock, T. D. (2015). Sulfur-controlled iron isotope fractionation experiments of core formation in planetary bodies. *Geochimica et Cosmochimica Acta*, *150*, 253–264. https://doi.org/10.1016/j.gca.2014.08.011

Sharp, Z. D., Shearer, C. K., McKeegan, K. D., Barnes, J. D., & Wang, Y. Q. (2010). The Chlorine isotope composition of the Moon and implications for an anhydrous mantle. *Science*, *329*, 1050–1053. https://doi.org/10.1126/science.1192606

She, J.-X., Wang, T., Liang, H.-D., Muhtar, M. N., Li, W., & Liu, X. (2019). Sn isotope fractionation during volatilization of Sn(IV) chloride: Laboratory experiments and quantum mechanical calculations. *Geochimica et Cosmochimica Acta*, *269*, 184–202.

Siebert, J., Corgne, A., & Ryerson, F. J. (2011). Systematics of metal-silicate partitioning for many siderophile elements applied to Earth's core formation. *Geochimica et Cosmochimica Acta*, *75*, 1451–1489. https://doi.org/10.1016/j.gca.2010.12.013

Siebert, J., Malavergne, V., Guyot, F., Combes, R., & Martinez, I. (2004). The behaviour of sulphur in metal–silicate core segregation experiments under reducing conditions. *Physics of the Earth and Planetary Interiors*, *143–144*, 433–443. https://doi.org/10.1016/j.pepi.2003.07.022

Siebert, J., Sossi, P. A., Blanchard, I., Mahan, B., Badro, J., & Moynier, F. (2018). Chondritic Mn/Na ratio and limited post-nebular volatile loss of the Earth. *Earth and Planetary Science Letters*, *485*, 130–139. https://doi.org/10.1016/j.epsl.2017.12.042

Sossi, P. A., Moynier, F., & Van Zuilen, K. (2018). Volatile loss following cooling and accretion of the Moon revealed by chromium isotopes. *Proceedings of the National Academy of Sciences of the United States of America*, *115*, 10920–10925. https://doi.org/10.1073/pnas.1809060115

Sossi, P. A., Nebel, O., O'Neill, H. S. C., & Moynier, F. (2017). Zinc isotope composition of the Earth and its behaviour during planetary accretion. *Chemical Geology*, *477*, 73–84.

Steenstra, E. S., Berndt, J., Klemme, S., Fei, Y., & van Westrenen, W. (2020). A possible high-temperature origin of the Moon and its geochemical consequences. *Earth and Planetary Science Letters*, *538*, 116222. https://doi.org/10.1016/j.epsl.2020.116222

Steenstra, E. S., Dankers, D., Berndt, J., Klemme, S., Matveev, S., & van Westrenen, W. (2019). Significant depletion of volatile elements in the mantle of asteroid Vesta due to core formation. *Icarus*, *317*, 669–681. https://doi.org/10.1016/j.icarus.2018.08.020

Steenstra, E. S., Rai, N., Knibbe, J. S., Lin, Y. H., & van Westrenen, W. (2016). New geochemical models of core formation in the Moon from metal-silicate partitioning of 15 siderophile elements. *Earth and Planetary Science Letters*, *441*, 1–9. https://doi.org/10.1016/j.epsl.2016.02.028

Steenstra, E. S., Seegers, A. X., Putter, R., Berndt, J., Klemme, S., Matveev, S., et al. (2020). Metal-silicate partitioning systematics of siderophile elements at reducing conditions: A new experimental database. *Icarus*, *335*, 113391. https://doi.org/10.1016/j.icarus.2019.113391

Steenstra, E. S., Sitabi, A. B., Lin, Y. H., Rai, N., Knibbe, J. S., Berndt, J., et al. (2017). The effect of melt composition on metal-silicate partitioning of siderophile elements and constraints on core formation in the angrite parent body. *Geochimica et Cosmochimica Acta*, *212*, 62–83. https://doi.org/10.1016/j.gca.2017.05.034

Suer, T. A., Siebert, J., Remusat, L., Menguy, N., & Fiquet, G. (2017). A sulfur-poor terrestrial core inferred from metal–silicate partitioning experiments. *Earth and Planetary Science Letters*, *469*, 84–97. https://doi.org/10.1016/j.epsl.2017.04.016

Thibault, Y., & Walter, M. J. (1995). The influence of pressure and temperature on the metal-silicate partition coefficients of nickel and cobalt in a model C1 chondrite and implications for metal segregation in a deep magma ocean. *Geochimica et Cosmochimica Acta*, *59*(5), 991–1002. https://doi.org/10.1016/0016-7037(95)00017-8

Tucker, J. M., & Mukhopadhyay, S. (2014). Evidence for multiple magma ocean outgassing and atmospheric loss episodes from mantle noble gases. *Earth and Planetary Science Letters*, *393*, 254–265. https://doi.org/10.1016/j.epsl.2014.02.050

Tuller-Ross, B., Marty, B., Chen, H., Kelley, K. A., Lee, H., & Wang, K. (2019). Potassium isotope systematics of oceanic basalts. *Geochimica et Cosmochimica Acta*, *259*, 144–154. https://doi.org/10.1016/j.gca.2019.06.001

Urey, H. C. (1947). The thermodynamic properties of isotopic substances. *Journal of the Chemical Society*, *0*, 562–581. https://doi.org/10.1039/jr9470000562

Vogel, A. K., Jennings, E. S., Laurenz, V., Rubie, D. C., & Frost, D. J. (2018). The dependence of metal-silicate partitioning of moderately volatile elements on oxygen fugacity and Si contents of Fe metal: Implications for their valence states in silicate liquids. *Geochimica et Cosmochimica Acta*, *237*, 275–293. https://doi.org/10.1016/j.gca.2018.06.022

Wade, J., & Wood, B. J. (2005). Core formation and the oxidation state of the Earth. *Earth and Planetary Science Letters*, *236*, 78–95. https://doi.org/10.1016/j.epsl.2005.05.017

Wang, K., & Jacobsen, S. B. (2016). Potassium isotopic evidence for a high-energy giant impact origin of the Moon. *Nature*, *538*, 487–490. https://doi.org/10.1038/nature19341

Wang, X., Amet, Q., Fitoussi, C., & Bourdon, B. (2018). Tin isotope fractionation during magmatic processes and the isotope composition of the bulk silicate Earth. *Geochimica et Cosmochimica Acta*, *228*, 320–335. https://doi.org/10.1016/j.gca.2018.02.014

Wang, X., Fitoussi, C., Bourdon, B., Fegley, B., & Charnoz, S. (2019). Tin isotopes indicative of liquid–vapour equilibration and separation in the Moon-forming disk. *Nature Geoscience*, *12*, 707–711. https://doi.org/10.1038/s41561-019-0433-4

Wang, Z., & Becker, H. (2013). Ratios of S, Se and Te in the silicate Earth require a volatile-rich late veneer. *Nature*, *499*, 328–331. https://doi.org/10.1038/nature12285

Wang, Z., Laurenz, V., Petitgirard, S., & Becker, H. (2016). Earth's moderately volatile element composition may not be chondritic: Evidence from In, Cd and Zn. *Earth and Planetary Science Letters*, *435*, 136–146. https://doi.org/10.1016/j.epsl.2015.12.012

Wasson, J. T., Kallemeyn, G. W., Runcorn, S. K., Turner, G., & Woolfson, M. M. (1988). Compositions of chondrites. *Philosophical Transactions of the Royal Society A Mathematical, Physical and Engineering Sciences*, *325*, 535–544. https://doi.org/10.1098/rsta.1988.0066

Wood, B. J., & Halliday, A. N. (2010). The lead isotopic age of the Earth can be explained by core formation alone. *Nature*, *465*, 767–770. https://doi.org/10.1038/nature09072

Wood, B. J., Smythe, D. J., & Harrison, T. (2019). The condensation temperatures of the elements: A reappraisal. *American Mineralogist*, *104*, 844–856. https://doi.org/10.2138/am-2019-6852ccby

Wood, B. J., Walter, M. J., & Wade, J. (2006). Accretion of the Earth and segregation of its core. *Nature*, *441*, 825–833. https://doi.org/10.1038/nature04763

Young, E. D., Shahar, A., Nimmo, F., Schlichting, H. E., Schauble, E. A., Tang, H., & Labidi, J. (2019). Near-equilibrium isotope fractionation during planetesimal evaporation. *Icarus*, *323*, 1–15. https://doi.org/10.1016/j.icarus.2019.01.012

References From the Supporting Information

Andrault, D., Bolfan-Casanova, N., Nigro, G. L., Bouhifd, M. A., Garbarino, G., & Mezouar, M. (2011). Solidus and liquidus profiles of chondritic mantle: Implication for melting of the Earth across its history. *Earth and Planetary Science Letters*, *304*(1–2), 251–259. https://doi.org/10.1016/j.epsl.2011.02.006

Bohlen, S. R., & Boettcher, A. (1982). The quartz–coesite transformation: A precise determination and the effects of other components. *Journal of Geophysical Earth*, *87*(B8), 7073–7078. https://doi.org/10.1029/jb087ib08p07073

Fiquet, G., Auzende, A. L., Siebert, J., Corgne, A., Bureau, H., Ozawa, H., & Garbarino, G. (2010). Melting of Peridotite to 140 Gigapascals. *Science*, *329*(5998), 1516–1518. https://doi.org/10.1126/science.1192448

Frost, D. J., Poe, B. T., Trønnes, R. G., Liebske, C., Duba, A., & Rubie, D. C. (2004). A new large-volume multianvil system. *Physics of the Earth and Planetary Interiors*, *143*(1–2), 507–514. https://doi.org/10.1016/j.pepi.2004.03.003

Kendall, J. D., & Melosh, H. J. (2016). Differentiated planetesimal impacts into a terrestrial magma ocean: Fate of the iron core. *Earth and Planetary Science Letters*, *448*, 24–33. https://doi.org/10.1016/j.epsl.2016.05.012

Lherm, V., & Deguen, R. (2018). Small-scale metal/silicate equilibration during core formation: The influence of stretching enhanced diffusion on mixing. *Journal of Geophysical Earth: Solid Earth*, *123*, 10496–10516. https://doi.org/10.1029/2018jb016537

Lloyd, E. C. (1971). *Accurate Characterization of the High-Pressure Environment: Proceedings* (Vol. 13). US National Bureau of Standards.

Rubie, D. C. (1999). Characterizing the sample environment in multianvil high-pressure experiments. *Phase Transitions*, *68*, 431–451. https://doi.org/10.1080/01411599908224526

Siebert, J., Badro, J., Antonangeli, D., & Ryerson, F. J. (2012). Metal-silicate partitioning of Ni and Co in a deep magma ocean. *Earth and Planetary Science Letters*, *321–322*, 189–197. https://doi.org/10.1016/j.epsl.2012.01.013

Woodland, A. B., & Angel, R. J. (1997). Reversal of the orthoferrosilite-high-P clinoferrosilite transition, a phase diagram for $FeSiO_3$ and implications for the mineralogy of the Earth's upper mantle. *European Journal of Mineralogy*, *9*, 245–254. https://doi.org/10.1127/ejm/9/2/0245

Woodland, A. B., & O'Neill, H. S. (1993). Synthesis and stability of (Fe2+)3(Fe3+)2–Si_3O_{12} garnet and phase relations with $Fe_3Al_2Si_3O_{12}$–(Fe2+)3(Fe3+)2–Si_3O_{12} solutions. *American Mineralogist*, *78*(9–10), 1002–1015.

Yagi, T., Akaogi, M., Shimomura, O., Suzuki, T., & Akimoto, S.-I. (1987). In situ observation of the olivine-spinel phase transformation in Fe_2SiO_4 using synchrotron radiation. *Journal of Geophysical Earth*, *92*(B7), 6207–6213. https://doi.org/10.1029/jb092ib07p06207

Yagi, T., & Akimoto, S.-I. (1976). Direct determination of coesite-stishovite transition by in-situ X-ray measurements. *Tectonophysics*, *35*(1–3), 259–270. https://doi.org/10.1016/0040-1951(76)90042-1